AN ABSTRACT OF THE THESIS OF

Robyn C. Boeke for the degree of Master of Science in Atmospheric Sciences presented on May 21, 2009.

Title: Biases in Droplet Radii and Optical Depths of Marine Stratocumulus Retrieved from MODIS Imagery.

Abstract approved:

James A. Coakley, Jr.

The 2007 Intergovernmental Panel on Climate Change assessment established that the effect of clouds on climate contributes the largest uncertainty in predicting the future climate. Satellite observations provide an opportunity for learning about the behavior of clouds. This thesis seeks to assess the accuracy of cloud properties retrieved from multispectral satellite imagery and test the usefulness of satellite data in verifying conclusions based on aircraft observations that marine stratus appear to be formed through the nearly adiabatic ascent of moist air. Retrievals of cloud optical depth, a measure of cloud thickness, using 0.64-μm reflectances and droplet radii using separately 1.6, 2.1, and 3.7-μm reflectances were obtained with the MODerate-resolution Imaging Spectroradiometer (MODIS). Owing to different amounts of

absorption by liquid water in the near infrared, with the least at 1.6 μm and the most at 3.7 μm, the growth of droplet radius with cloud thickness should result in the largest droplet radii retrieved using the 3.7-μm reflectances and the smallest using 1.6-μm reflectances. Droplet radii retrieved using the 2.1-μm reflectances, however, are often the largest, and those retrieved using 3.7-μm reflectances are often the smallest. In addition aircraft observations indicate that the relationships between droplet radius, r_e, and optical depth, τ, $d \ln r_e / d \ln \tau$,should be approximately equal to 0.2 for marine stratocumulus. While satellite observations in optically thick, overcast regions yielded $d \ln r_e / d \ln \tau$ consistent with this result, retrievals for regions with broken clouds often yielded $d \ln r_e / d \ln \tau$ substantially smaller than 0.2.

Clouds often exhibit large horizontal and vertical variability. In this thesis a simple radiative transfer model was used to predict reflectances at visible and near infrared wavelengths for clouds formed through the adiabatic ascent of moist air, and then a retrieval scheme based on vertically uniform clouds was used to determine if the departures from the behavior expected for adiabatic clouds might be caused by the assumption of spatial uniformity used in the retrievals. The simulations indicated that at all cloud thicknesses the progression of droplet size using 1.6, 2.1, and 3.7-μm reflectances followed that suggested by the absorptive properties of liquid water. The simulation also indicated, however, contrary to the observations, that when the clouds were optically thin, $d \ln r_e / d \ln \tau$ should be greater than 0.2, the value expected for the adiabatic ascent of moist air.

The simulation was adapted to account for the effects of horizontal variations within clouds. Each 1-km pixel was given a subpixel distribution of optical depths based on a gamma distribution with mean taken from MODIS pixel-scale optical depths and variance given by Kato et al. (2006), obtained from Large Eddy Simulations of marine stratocumulus. Each subpixel was allowed to develop vertically following the adiabatic ascent of moist air. The average of the reflectances for the subpixels was used to retrieve the cloud properties for the pixels, and these properties were compared with the average properties of the subpixels. The retrievals obtained using 1.6-μm reflectances were most strongly affected by the addition of subpixel variations in optical depth and droplet radius. Mean droplet radius retrieved in the simulation was largest when using 1.6-μm reflectances, followed by that retrieved using 2.1 and 3.7-μm reflectances. The simulation of large droplet radii at the shorter wavelengths indicated that the large droplets observed in MODIS may result from horizontal variations within the 1-km MODIS pixel. The values of $d \ln r_e / d \ln \tau$ calculated for horizontally heterogeneous clouds were close to 0.2, but showed variations that extend both above and below this value, consistent with the MODIS observations.

To illustrate the findings based on the simulations, visible optical depth and droplet radius were retrieved for MODIS 500-m pixels overcast by marine stratocumulus. The 500-m pixels were used to represent the subpixel variability within 2-km pixels constructed from the 500-m pixels. Differences between cloud properties retrieved using average radiances and averages of the subpixel properties were compared for overcast and broken-cloud regions using both MODIS and the

Partly Cloudy Pixel Retrieval (PCPR) schemes for identifying the overcast 2-km pixels. In the regions overcast by optically thick marine stratocumulus, both methods of identifying overcast pixels led to small biases in the retrieved droplet radii and optical depths. Values of $d \ln r_e / d \ln \tau$ obtained in the overcast regions using the PCPR identifications were closer to the value of 0.2 expected for adiabatic clouds than those obtained using MODIS identifications. Additionally, values of $d \ln r_e / d \ln \tau$ calculated using the 500-m overcast pixels yielded better results than those calculated using the 2-km pixels. In regions containing broken clouds, the PCPR identification provided a smaller bias than the MODIS identification, however both methods showed greater biases than those calculated for regions overcast by optically thick marine stratocumulus. Values of $d \ln r_e / d \ln \tau$ for the regions containing broken clouds showed a positive value when using the PCPR scheme to identify overcast pixels, and a negative value when using the MODIS cloud mask to identify overcast pixels. Consistent with the results from the overcast regions, the $d \ln r_e / d \ln \tau$ obtained for the 500-m overcast pixels were in closer conformity with adiabatic clouds than the values obtained for the 2-km pixels using both the MODIS and PCPR identifications.

Biases in Droplet Radii and Optical Depths of Marine Stratocumulus Retrieved from MODIS Imagery

by

Robyn C. Boeke

A THESIS

submitted to

Oregon State University

in partial fulfillment of
the requirements for the
degree of

Master of Science

Presented May 21, 2009

Commencement June 2010

Master of Science thesis of Robyn C. Boeke presented on May 21, 2009.

APPROVED:

Major Professor, representing Atmospheric Sciences

Dean of the College of Oceanic and Atmospheric Sciences

Dean of the Graduate School

I understand that my thesis will become part of the permanent collection of Oregon State University libraries. My signature below authorizes release of my thesis to any reader upon request.

Robyn C. Boeke, Author

ACKNOWLEDGEMENTS

The first person I would like to thank is my advisor, Dr. Jim Coakley. I don't think I ever quite understood the meaning of the words 'hard work', 'dedication', or 'attention to detail' until I met Jim. He has helped me to develop myself in these areas and more during my time here at Oregon State University, and I've never felt as capable and ready to seize the day as I have under his tutelage. He sets a superhuman example of a professor, advisor, coworker, and scientist, and I feel unbelievably lucky to have been given the opportunity to learn from him. Thanks, Jim, for always challenging me and helping me see that I can accomplish anything I set my mind to.

Next, I would like to thank Bill Tahnk and Dan Brown for their invaluable advice and support. Bill is a dictionary of knowledge on everything from classes, IDL, data analysis, and even the best places to hike. I'd like to thank him for his patience in answering my questions and for his numerous pep talks along the way. Dan Brown is my fellow student and has been an excellent study partner, but most of all, he's been a great friend. Thanks, Dan, for your listening ear, and may the force be with you.

I would like to thank Drs. Eric Skyllingstad, Karen Shell, and Jeff Nason for serving on my committee, as well as NASA Grant NNX08AG01G for providing funding.

Last (but definitely not least), I would like to thank my family for their love and support. Mom and Dad, I can't even begin to put into words my gratitude for all you have done. A heartfelt thanks goes to my partner Adam for his love and encouragement, it has meant more to me than words can say. A special thanks goes to my dog Sunny, for his unconditional love, friendship, and hours of entertainment.

TABLE OF CONTENTS

TABLE OF CONTENTS (Continued)

LIST OF FIGURES

LIST OF FIGURES (Continued)

LIST OF FIGURES (Continued)

LIST OF FIGURES (Continued)

LIST OF TABLES

BIASES IN DROPLET RADII AND OPTICAL DEPTHS OF MARINE STRATOCUMULUS RETRIEVED FROM MODIS IMAGERY

CHAPTER 1

INTRODUCTION

1.1 Motivation

Clouds play a major role in Earth's radiation balance. They reflect a substantial portion of incident sunlight, and they absorb and emit a substantial fraction of outgoing longwave radiation. The Intergovernmental Panel on Climate Change (IPCC) Fourth Assessment Report (2007) concluded that clouds contribute a significant radiative forcing of climate on the global scale. Unfortunately, the level of scientific understanding of clouds and how they will respond and contribute to climate change is low. A knowledge of clouds will be crucial in predicting the future climate because small changes in cloud properties lead to major changes in climate (IPCC 2007). The accurate determination of cloud properties is imperative because they are often used to calculate the radiation budget and assess the climate response to forcings. If the cloud properties are not sound, then the progress towards reliable prediction of cloud behavior is hampered.

While the net effect of clouds on climate is cooling, high clouds, such as cirrus, and low clouds, such as marine stratus, have opposite impacts on the radiation budget. High, thin clouds have a warming effect because incident sunlight passes through them but longwave radiation emitted by the Earth's surface and lower atmosphere is absorbed and only a portion is re-emitted. Low clouds tend to be thicker and are

composed of water droplets. They have relatively large albedos, meaning more incident sunlight is reflected and less is transmitted to the surface. Marine stratocumulus have a small greenhouse forcing because they do not change the top-of-atmosphere longwave emission significantly. They are at such low altitudes that their emission temperatures are almost the same as those of the surface. The dominant effect on the Earth's radiation budget is on the reflection of sunlight, so that the net effect of low-level clouds is cooling.

The impact of low clouds on the earth's energy budget is larger than that of high clouds. Low clouds account for most oceanic cloud cover and the oceans cover over 70% of earth's surface, making low clouds the most prevalent cloud system. Observations compiled by Hartmann et al. (1992) indicate that low clouds also contribute the greatest amount to net cloud forcing, an average of -16 Wm^{-2} out of -22 Wm^{-2} total cloud forcing. Low clouds are also sensitive to the availability of cloud condensation nuclei (CCN) and may be strongly affected by anthropogenic forcing through the burning of fossil fuels. Knowledge of cloud microphysical and optical properties for marine stratocumulus is expected to lead to a better understanding of the links between clouds and climate.

An adiabatic cloud is one in which droplet radius, optical depth, and liquid water content are linked to cloud thickness, with liquid water content increasing linearly with height above the lifting condensation level. Aircraft observations have shown that the adiabatic parcel model represents the vertical structure of marine stratocumulus (Brenguier et al. 2000, Miles et al. 2000). In addition, several studies

have used satellite retrievals as a means to discover the relationships between cloud properties, and the adiabatic model is often found to be a good predictor of cloud behavior (Szczodrak et al. 2001, Schüller et al. 2003). An adiabatic model modified to account for the non-adiabatic effects of mixing has also been proposed by Boers et al. (2006). This thesis re-examines satellite observations by using retrievals from the Moderate-resolution Imaging Spectroradiometer (MODIS) imagery to determine the validity of the adiabatic parcel model in understanding the behavior of marine stratocumulus.

Many methods for inferring cloud properties are based on an assumption that clouds are vertically and horizontally uniform, even though the properties of most clouds vary both vertically and horizontally. Droplet radius and optical depth of marine stratus retrieved from MODIS often fail to coincide with the relationships expected on the basis of adiabatic parcel models. When light hits a cloud droplet, it can be either scattered or absorbed. Optical depth is a non-dimensional parameter used to measure the exponential extinction of light within a medium. The optical depth increases as the medium becomes thicker. For clouds formed through the adiabatic ascent of moist air droplet radii grow from cloud base to cloud top. Consequently, owing the relatively strong absorption at longer wavelengths, the largest droplets are expected to be retrieved when using 3.7-μm reflectances because light is quickly extinguished at this wavelength. Droplet radii retrieved using 3.7-μm reflectivities are thus representative of droplets near cloud tops. The smallest droplets are expected to be observed when using the 1.6-μm reflectances because light

penetrates deeper into the cloud at the shorter wavelength since absorption by water is relatively small. 1.6-μm reflectivity is thus representative of the smaller droplets deeper in the cloud. MODIS retrievals, however, often indicate the presence of large droplets retrieved using both 1.6 and 2.1-μm reflectivities, and somewhat smaller droplets retrieved using the 3.7-μm reflectances. This departure from trends expected for adiabatic clouds arises because the assumption that pixels are overcast is frequently violated (Platnick et al. 2003, Coakley et al. 2005). MODIS fields of view are assumed to be completely covered by clouds, but often they are only partially covered. The influence of optically thin areas may contribute to the departure of cloud properties from those expected for adiabatic ascent of moist air when pixels are only partly cloudy, as noted by Szczodrak et al.(2001) and Schüller et al. (2005). This thesis contends that the departure of cloud properties from expected values also occurs because of variations of cloud properties within the 1-km MODIS pixels.

An adiabatic cloud model was developed and used to study the sensitivity of retrieved cloud properties to the vertical profile of the properties within MODIS 1-km pixels. A simple radiative transfer code computed reflectances for a multilayered cloud in which the properties changed with altitude. Droplet radii and optical depths were retrieved assuming that the cloud was vertically uniform. The optical depths and cloud top droplet radii for clouds with vertical structure were compared to the retrieved optical depths and droplet radii assuming vertically uniform clouds. The simulations tested whether the departures of the MODIS retrievals from those

expected for the adiabatic ascent of moist air could be attributed to the assumption that clouds were vertically uniform.

As accounting for the vertical profiles of droplet radius within clouds failed to explain the MODIS observations, the effects of horizontal variations on retrieved cloud properties were studied. Analyses of satellite imagery in conjunction with space-based lidar observations have shown that the expected adiabatic relationships between droplet radius and optical depth hold for MODIS 1-km pixels overcast by optically thick marine stratus (Hayes et al., 2009), but departures from the adiabatic values existed for pixels overcast by optically thin marine stratus and for partly cloudy pixels. To examine the effect of horizontal variations, the pixel used in the radiative transfer model was divided into subpixels of clouds having varying heights so as to obtain representative distributions of cloud optical depths within the pixel. The clouds in each subpixel were allowed to grow adiabatically to achieve the prescribed optical depth. The retrievals for droplet radius and optical depth based on the horizontally uniform model were compared with the average of the retrieved pixel properties for the horizontally varying cloud within the pixel. The subpixel variation in optical depth was represented by a gamma distribution with mean provided by MODIS retrievals of pixel-scale optical depths for marine stratocumulus and variance given by Kato et al. (2006) based on Large Eddy Simulations of marine stratocumulus.

The MODIS observations used in this study were drawn from 50-km regions that contained a single layer of marine stratocumulus with no other clouds present. The Partly Cloudy Pixel Retrievals (Coakley et al. 2005) provided information on

cloud fraction, altitude, cloud optical depth, and droplet radii derived using the three near-infrared wavelengths from the Terra MODIS. The Partly Cloudy Pixel Retrieval (PCPR) scheme was developed to account for pixels with partial cloud cover and is used to identify pixels as either overcast, partly cloudy, or cloud-free. It is applied to pixels containing a single layer of marine stratocumulus. The retrieved cloud properties were used to assess whether observations of marine stratus could be described by the adiabatic parcel model.

1.2 Background

Several methods for retrieving cloud properties from satellite observations have been developed, though most invoke the assumption of a vertically uniform cloud. Nakajima and King (1990) sought to retrieve droplet radius for homogeneous clouds and were the first to find the occurrence of multiple solutions for droplet radius at a given optical depth for a given pair of visible and near infrared reflectivities. The retrieval algorithm calculated a droplet radius, r_e, and optical thickness, τ, that best fit the observed near infrared and visible reflectivities, but when τ and r_e were small, multiple solutions frequently occurred. They arose because 1) the relationships between reflectivity and cloud properties are nonlinear, and 2) optical depth is weakly dependent on droplet radius, so that for small τ and r_e a solution exists that gives the same reflectances as obtained for a given optical depth and more than one droplet radius. Nakajima and King were able to avoid multiple solutions by performing

retrievals using the visible and two or three near infrared reflectivities instead of just the visible and a single near infrared reflectivity. Alternately, the small droplet radius solutions were removed by setting a lower bound for retrieved droplet radius, in which case the solution with the larger droplet radius was always chosen. The advantage of the Nakajima and King retrieval scheme is that it can be applied in principle to any cloud to obtain an optical depth and droplet radius. The disadvantage is that it does not give useful information about the vertical profile of droplet radius within clouds.

A study by Schüller et al. (2004) used an adiabatic model proposed by Brenguier et al. (2000) to interpret the retrieved droplet radius and optical depths obtained with the Nakajima and King algorithm in terms of droplet number concentration and cloud geometric thickness. The motivation for this analysis was that in convective clouds, droplet radius is a function of both number concentration and cloud thickness. Schüller et al. sought to determine whether changes in droplet effective radius could be attributed to changes in droplet number concentration or cloud geometric thickness. The droplet radius provided by the Nakajima and King method is an "equivalent" radius, the radius that a vertically and horizontally uniform cloud would produce. The actual droplet radius within the cloud could depart considerably from the retrieved value. The profile of droplet radius within an adiabatic cloud was used to calculate visible and near infrared reflectivities and geometric thickness and number concentration were adjusted to obtain the observed reflectivities. Using droplet size distributions matched closely to those observed by aircraft as opposed to those typically used in satellite-based retrievals produced

retrieved adiabatic "equivalent" droplet number concentrations and geometric heights that were reasonably accurate.

With the goal of accurately representing the vertical structure of cloud properties, Chang and Li (2003) used the MODIS reflectivities for the three near infrared wavelengths to infer a profile of droplet radius. The principle behind their study was that liquid water droplets retrieved using different wavelengths had different absorptive properties. The relatively large absorption at 3.7 μm causes the near infrared reflectance to saturate at a relatively small optical depth. Once saturation is achieved, the reflectance becomes independent of optical depth. Photons that penetrate to low levels in the cloud are absorbed. Consequently, the reflected light comes only from the topmost cloud layers. Droplet radius retrieved at this wavelength will be more representative of the cloud-top droplet radius. At 1.6 μm, absorption by liquid water is smaller, and so saturation is reached at a greater optical depth. The droplet radius retrieved using 1.6-μm reflectances is representative of those at lower layers in the cloud. The droplet radii retrieved at different wavelengths form the basis for the vertical distribution of droplet size inferred by Chang and Li. They fit three analytic profiles of droplet radius to the data to determine the best fit for the droplet vertical profile: the first in which droplet radius was linearly proportional to optical depth ($dr_e/d\tau$ = constant), a second in which droplet radius grew linearly with height above the LCL, (dr_e/dz' = constant, where z' is height), and a third in which liquid water content LWC was proportional to height z ($dLWC/dz$ = constant). The first two profiles were chosen to replicate what in-situ measurements have shown (Miles et al.

2000), and the third profile represented an adiabatic cloud. Regardless of the profile used in the retrieval, Chang and Li inferred that cloud droplet radius sometimes increased from cloud base to cloud top, and sometimes decreased from cloud base to cloud top. The occurrence of larger droplets at cloud base was attributed to light drizzle occurring near cloud base, or the existence of ice-phase particles, which have a higher absorptivity than liquid water (Pilewskie and Twomey 1987). Additionally, the survey of aircraft observations reported by Miles et al (2000) indicated that the pattern of increasing droplet radii with height occurs predominantly for marine stratus, and the pattern of decreasing droplet radii with height is observed in continental stratus. Chang and Li performed their retrievals for clouds over Oklahoma.

A study by Boers et al. (2006) added complexity to the retrieval scheme by taking into account mixing and the subadiabatic character of many water clouds. They started with a single-layered, non-adiabatic cloud with a smooth liquid water profile. Unlike previous studies, Boers et al. included the entrainment of the relatively dry air that overlies marine stratocumulus in the model. Mixing between cloud and the dry air can affect the number concentration, N, and volume radius, r_v, both of which determine the liquid water content, LWC, of clouds. The effects of mixing can cause the profile of liquid water content to deviate from that for an adiabatic cloud. To quantify this effect, Boers et al. used two mixing models, homogeneous and inhomogeneous mixing. In homogeneous mixing, the entrained air evaporates cloud droplets at an equal rate regardless of the radius of the droplet in a way that preserves the droplet number concentration. The increase of supersaturation with height above

the lifting condensation level leads to more droplets, balancing out the loss of droplets to evaporation. The net effect, however, is that the volume radius decreases. In inhomogeneous mixing, the entrained air evaporates some of the cloud droplets and leaves others unaffected so as to preserve volume radius and decrease number concentration. The mixed air simply dilutes the cloud, and in this case, a nonadiabatic cloud will behave like an adiabatic cloud, only with less liquid water. The properties of an adiabatic cloud are linked through simple thermodynamic equations, and therefore a change in the size distribution or number concentration is likely to affect all properties in tandem. Boers et al. used number concentration and geometric height in terms of droplet radius, optical depth, and two other constants A_1 and A_2, which depended in various ways on the effects of mixing. With this additional complexity, Boers et al. discovered that retrievals of cloud geometric thickness were not sensitive to which mixing model was used. The vertically-averaged droplet number concentrations were not sensitive to the type of mixing model used, but cloud base number concentrations were strongly affected by the liquid water content. Without detailed information on any particular atmospheric event, it is difficult to determine the governing mixing model. Based on aircraft measurements during the second Dynamics and Chemistry of Marine Stratocumulus (DYCOMS-II) experiment in 2001, Burnet and Brenguier (2007) observed that stratocumulus clouds follow some path intermediate between the two extremes of homogeneous and inhomogeneous mixing.

While the number concentration retrievals in Boers et al. were subject to error, several conclusions were drawn. The retrieved droplet number concentrations were sensitive to the mixing model. Number concentrations were also affected by the liquid water profile, especially near the cloud base, suggesting that deviations of the liquid water profile from that for an adiabatic parcel affected the retrieved cloud properties. Since cloud microphysical properties are linked, a sensitivity to the entrainment of dry air may strongly affect droplet radius as well as number concentration. Nonetheless, Boers et al. ran their model with several different realistic variations in mixing and liquid water profiles and found that the retrieved droplet number concentration varied by 17-20%.

Hayes et al (2009) obtained cloud properties using MODIS observations by relying on 532-nm attenuated backscatter coefficients obtained with the Cloud-Aerosol Lidar and Infrared Pathfinder Satellite Observation (CALIPSO) lidar to identify which MODIS pixels were overcast by marine stratus and which contained broken clouds. The goal was to identify differences in the cloud properties derived for overcast and broken-cloud regions, and to assess whether the relationships predicted by the adiabatic model held for both overcast and broken-cloud regions. Hayes et al. (2009) found that the retrieved optical depths from Aqua MODIS for areas that were only partly cloudy were smaller than those for clouds in regions that were overcast, while the retrieved droplet radii were larger than those for the overcast regions. The pixel-scale mean and standard deviation of the optical depths retrieved for pixels overcast by optically thick clouds drawn from 660 50-km scale regions overcast by

marine stratus was 15.71 ± 8.22, and for pixels overcast by broken clouds from 460 regions was 6.88 ± 5.13. Droplet radius retrieved for the overcast pixels in the broken cloud regions using 1.6-μm reflectivities was 1.68 μm larger than those retrieved for the overcast regions. A similar departure was observed when using both the 2.1 and 3.7-μm reflectances. For overcast regions, the $d \ln r_e / d \ln \tau$ values were 0.174 for droplet radii retrieved using 1.6-μm reflectivities, 0.201 using 2.1-μm reflectivities, and 0.188 when using 3.7-μm reflectivities. These are reasonably close to the value 0.2 expected for clouds behaving adiabatically. They found however that the relationship broke down when pixels contained optically thin clouds. When regions with only partial cloud cover were included, the $d \ln r_e / d \ln \tau$ values were 0.027 for droplet radii retrieved using 1.6-μm reflectivities, 0.094 for 2.1-μm reflectivities, and 0.179 for 3.7-μm reflectivities. In the broken-cloud regions, these departures may have occurred because either the clouds were not adiabatic, or the retrievals were somehow incorrect.

In this study, the droplet radii and visible optical depths of marine stratus and stratocumulus as inferred from MODIS imagery were analyzed. The motivation for this study was to find the relationships predicted by the adiabatic parcel models in satellite imagery data. For adiabatic clouds the droplet radius retrieved using the 3.7-μm reflectivity should be largest, the droplet radius retrieved using the 2.1-μm reflectivity should be somewhat smaller, and the radius retrieved using the 1.6-μm reflectivity should be the smallest. The results of Hayes et al. for broken cloud regions showed that that the 2.1-μm derived droplet radius was largest, followed by the

3.7-μm and 1.6-μm derived radii. Likewise, the values of $d \ln r_e / d \ln \tau$ were close to 0.2 for optically thick marine stratus, but diverged from this value for broken and optically thin clouds. The goal of this study was to explain such results.

CHAPTER 2

RADIATIVE PROPERTIES OF ADIABATIC CLOUDS

2.1 Adiabatic Relationships for Marine Stratocumulus

Cloud formation occurs in the presence of micron to sub-micron wettable particles called cloud condensation nuclei (CCN). As these cloud particles are lifted above the lifting condensation level, they are cooled by adiabatic ascent. The adiabatic cooling is accompanied by an increase in the relative humidity, and water begins to condense onto the CCN as they gain altitude. The air becomes supersaturated when relative humidity exceeds 100%. Cloud droplets grow as water continues to condense on them. The increase in liquid water content (*LWC*) with height for adiabatic ascent is linear, which results from the first law of thermodynamics, the hydrostatic approximation, and the Ideal Gas Law. The change in adiabatic liquid water content, *dLWC*, can be represented in the adiabatic form of the first law by

$$c_p dT - L_{lv} dLWC - v dP = 0, \tag{1}$$

where c_p is the specific heat of dry air at constant pressure, dT is the change in temperature, L_{lv} is the latent heat of vapor-to-liquid conversion, v is the specific volume, and dP is the change in pressure. The terms add to zero because in an adiabatic process no heat is added or removed. According to hydrostatic balance,

$$\frac{dP}{dz} = -\rho g, \tag{2}$$

where ρ is the density of air and g is the gravitational acceleration constant. Substituting (2) into (1) for dP and solving for $dLWC$ gives

$$dLWC = \frac{c_p}{L_{lv}}\left(\frac{dT}{dz} + \frac{g}{c_p}\right)dz \tag{3}$$

The two terms in brackets represent two atmospheric lapse rates. The dry adiabatic lapse rate, $g / c_p \equiv \Gamma_d$, is constant. The saturated adiabatic lapse rate, $dT / dz \equiv \Gamma_s$, is relatively constant in marine stratocumulus clouds due to the limited vertical extent of these clouds. Consequently, the change in adiabatic liquid water content with height above the lifting condensation level is constant:

$$\frac{dLWC}{dz} = \frac{c_p}{L_{lv}}\left(\Gamma_s + \Gamma_d\right). \tag{4}$$

Using (4) and the definition of liquid water content,

$$LWC = \frac{4}{3}\pi\rho_w N r_v^3, \tag{5}$$

where ρ_w is the density of water, N is the droplet number concentration, which for adiabatic ascent is assumed to be constant, and r_v is the volume radius, droplet growth is given by

$$r_v^3(H) = BH + C. \tag{6}$$

Thus, the liquid water concentration increases linearly with height, H, above the lifting condensation level. Here B and C are constants found empirically using observations (Brenguier et al. 2003). B accounts for the rate of condensation with ascent and C accounts for the liquid water concentration at cloud base. In an adiabatic cloud, droplet radius increases as $H^{1/3}$. A parameter that will be used in this thesis is the

effective radius, given by the ratio of the third moment of the droplet size spectrum to the second moment of the droplet size spectrum. It is found by

$$r_e(z) = \frac{\int \pi r^3 n(r,z)dr}{\int \pi r^2 n(r,z)dr} \tag{7}$$

The volume radius is related to the effective radius by $r_v^3 = \kappa r_e^3$, where κ is approximately equal to 0.8. In this thesis, the difference between volume radius, r_v and effective radius, r_e will be ignored. The effective radius will be used in the remaining calculations.

The interaction of radiation with cloud droplets is measured in terms of an optical depth. Optical depth is a non-dimensional parameter that measures the exponential extinction of light in a medium. Often τ is taken to be zero at the top of the atmosphere, increasing downward. Optical depth is also related to *H,* the physical thickness of a cloud, and is given by:

$$\tau = \int_0^H N\sigma dh \tag{8}$$

where σ is the extinction cross section. Physically, the cross section represents the area each cloud droplet removes from the incident radiation. When radiation comes into contact with this area, it can either be scattered or absorbed. Since cloud droplets have radii that are much greater than the wavelengths associated with sunlight, σ is often approximated by $2\pi r_e^2$, giving

$$\tau = \int_0^H 2\pi N r_e^2(h)dh\,. \tag{9}$$

Substituting (6) into (8) and taking $r_e = r_v$ gives

$$\tau = \frac{6\pi N}{5B}[(BH + C)^{5/3} - C^{5/3}]. \tag{10}$$

Following Brenguier et al. (2003) and others, nucleation of droplets at the cloud base is often ignored, equivalent to setting $C = 0$. The optical depth is then given by

$$\tau = N\frac{6\pi}{5B}(BH)^{5/3}, \tag{11}$$

so that $\tau \propto H^{5/3}$. Here, (6) and (10) will be used to calculate droplet growth from cloud base to cloud top and optical depth assuming that the cloud is adiabatic.

Droplet radius and optical depth are correlated in an adiabatic cloud such that the ratio between them, $d\ln r_e / d\ln\tau \sim 0.2$ (Szczodrak et al. 2001, Boers et al. 2006). This value can be derived using

$$\tau = N^{1/3}H^{5/3} \text{ and } r_e = N^{1/3}H^{1/3}, \tag{12) and (13}$$

given in Boers et al. (2001) and Brenguier et al. (2000). Combining (11) and (12) the relationship between τ and r_e is given by

$$\tau = \frac{r_e^5}{N^{4/3}}, \text{ hence } \Delta\tau = \frac{5\Delta r_e r_e^4}{N^{4/3}}. \tag{14) and (15}$$

The relationship $d\ln r_e / d\ln\tau$ can be approximated by dividing both sides of the above equation by τ and simplifying:

$$\frac{\Delta\tau}{\tau} = \frac{5\Delta r_e}{r_e}, \tag{16}$$

then

$$\Delta\ln\tau = 5\Delta\ln r_e, \tag{17}$$

and finally

$$\frac{\Delta \ln r_e}{\Delta \ln \tau} \approx \frac{d \ln r_e}{d \ln \tau} = \frac{1}{5}. \tag{18}$$

If the cloud is adiabatic or liquid water content increases linearly with height, changes in r_e and τ should always maintain this relationship.

2.2 The Interaction of Solar Radiation and Cloud Particles

Radiation from the sun falls between 0.1 μm and 4 μm. When sunlight hits a cloud particle, it is either scattered or absorbed. The total extinction of light accounts for the attenuation due to both effects, and is described by the extinction cross-section σ. As mentioned in Section 2.1 σ represents the effective area an object blocks from the incident radiation. It is related to a droplet's geometric cross-section by

$$\sigma = Q_{ext} \pi r_e^2, \tag{19}$$

where πr_e^2 is the area of a spherical cloud droplet and Q_{ext} is the extinction efficiency for the cloud droplet. For cloud droplets and sunlight, Q_{ext} is greater than one, meaning that a droplet can extinguish more sunlight than is indicated by its geometric cross-section. In fact, for a typical droplet radius of 10 μm at visible wavelengths, $Q_{ext} \approx 2$ and $\sigma = 2\pi r_e^2$. The explanation for this lies in Mie Theory for spherical droplets, which describes the interaction of electromagnetic waves with atmospheric particles in terms of the size parameter, given by

$$x = \frac{2\pi r}{\lambda}, \tag{20}$$

where r is the particle radius and λ is the wavelength of the radiation. Q_{ext} is a strong function of x. For a particle with $x << 1$ (the particle radius is much smaller than the wavelength of incident radiation), light is scattered equally in all directions and Q_{ext} becomes proportional to x^4. For a particle with $x >> 1$, such as cloud droplets, strong forward scattering is observed. The strong forward scattering can be explained by the interaction of incident radiation with the edge of a particle. As sunlight hits the edge of a spherical cloud droplet, it is diffracted into the forward direction, thus the total light extinguished is the sum of the area blocked by the particle and the light diffracted by the particle edges. At visible wavelengths half of the extinction results from radiation being scattered in all directions and half is redirected as the diffraction peak in the direction of the incident light.

The effects of scattering and absorption on solar radiation are governed by the equation of transfer, given by

$$\mu \frac{dI(\mu,\phi)}{d\tau} = I(\mu,\phi) - \frac{\omega}{4\pi} \int_0^{2\pi} d\phi' \int_{-1}^{1} d\mu' p(\mu,\phi;\mu',\phi') I(\mu',\phi'), \tag{21}$$

where μ is the cosine of the zenith angle and ϕ is the azimuth angle measured in a plane perpendicular to the nadir direction. The terms in this equation, from left to right, are the change in radiance as it passes through a medium along a given direction (μ,ϕ), the incident radiance along the direction (μ,ϕ), and the contribution of scattering to the overall change in radiance in the direction of propagation. The scattering phase function in the equation of transfer, $p(\mu,\phi;\mu'\phi')$, represents the angular distribution of

scattered photons and is dependent on the properties of different types of atmospheric particles, such as haze particles, molecules, and cloud droplets. The phase function used here to represent the scattering of solar radiation by cloud droplets is represented by the asymmetry parameter, g, which is the average value of the cosine of the scattering angle. It is given by

$$g = \frac{1}{2}\int_{-1}^{1} \mu p(\mu) d\mu \,. \tag{22}$$

For scattering that is predominantly in the forward direction g approaches a value of 1, while for radiation that is predominantly backscattered, g approaches -1. If the scattering is completely symmetric, $g = 0$. For a typical cloud droplet, $g \approx 0.85$, but this value changes as droplet size changes.

The single scattering albedo, ω, is the fraction of incident radiation that is scattered by an atmospheric particle. It is given by the ratio of the scattering cross section to the extinction cross section and is given by

$$\omega = \frac{\sigma_{scattering}}{\sigma_{extinction}} \,. \tag{23}$$

The scattering cross section is the area of the incident radiation that is blocked by a scattering and absorbing object that is then scattered into all directions as given by the scattering phase function. The light blocked which is not scattered is then absorbed.

The asymmetry parameter g, single scattering albedo ω, and extinction cross section σ are all dependent on the wavelength of incident radiation and the size of the cloud droplet. These values are calculated using Mie Theory for the scattering and absorption by spherical droplets In this thesis the required parameters are used at the

four wavelengths of interest, 0.64, 1.6, 2.1, and 3.7 μm. Table 2.1 lists a subset of these values for 0.64 and 3.7 μm.

λ (μm)	**r_e (μm)**	**cross section (cm^2)**	**ω**	***g***
0.64	2	1.72E-07	1	0.79206
	3	3.73E-07	1	0.82153
	4	6.50E-07	1	0.83575
	5	1.00E-06	1	0.84371
	6	1.43E-06	1	0.84903
	8	2.51E-06	1	0.85601
	10	3.89E-06	1	0.86072
	12	5.57E-06	1	0.86404
	14	7.55E-06	1	0.86661
	16	9.83E-06	1	0.86834
	18	1.24E-05	1	0.8697
	20	1.53E-05	1	0.87107
	24	2.16E-05	1	0.8731
	28	2.98E-05	1	0.87463
	32	3.88E-05	1	0.87573
	40	6.04E-05	1	0.87739
3.7	2	1.64E-07	0.9785	0.78108
	3	4.98E-07	0.9751	0.79974
	4	9.10E-07	0.96748	0.79168
	5	1.34E-06	0.95718	0.77835
	6	1.80E-06	0.94561	0.76926
	8	2.91E-06	0.92336	0.77237
	10	4.36E-06	0.90489	0.79093
	12	6.15E-06	0.88927	0.81035
	14	8.26E-06	0.87524	0.82608
	16	1.07E-05	0.86218	0.83821
	18	1.34E-05	0.84985	0.84769
	20	1.64E-05	0.83811	0.85536
	24	2.34E-05	0.81628	0.86745
	28	3.15E-05	0.79638	0.87693
	32	4.09E-05	0.77818	0.8848
	40	6.32E-05	0.74618	0.89744

Table 2.1: Mie extinction cross sections, single scattering albedos, and asymmetry parameters for cloud droplets for radiation at 0.64 and 3.7 μm.

In order to treat multiple scattering, the equation of transfer is simplified using the Eddington Approximation. The Eddington Approximation begins with a form of the transfer equation that is for the azimuthally averaged component of the radiance. Upon Fourier decomposition, the transfer equation leads to equations that have the same form for all of the azimuthal components. The radiance for a given azimuthal component is broken down into a power series in μ, the cosine of the zenith angle:

$$I(\tau,\mu) = I_o(\tau) + I_1(\tau)\mu + I_2(\tau)\mu^2 + \ldots. \qquad (24)$$

The series is truncated at first order, so that $I(\tau,\mu)$ varies slowly with zenith angle. The Eddington Approximation holds for optically thick water clouds and will provide the relationships needed for this study.

A set of coupled differential equations are obtained by integrating each term in (23) over the cosine of the solar zenith angle, producing a zeroeth moment, first moment, and second moment. The mean intensity, I_o, is given by the zeroeth moment. The net radiative flux is related to the first moment. The net flux is the sum of the upward flux and downward flux, F^+ and F^-, given here by

$$F^+ = 2\pi\int_0^1 d\mu'\,\mu' I(\mu') \text{ and } F^- = 2\pi\int_{-1}^0 d\mu'\,\mu' I(\mu') \qquad (25) \text{ and } (26)$$

The coupled differential equations in the Eddington Approximation are

$$\frac{dF}{d\tau} = 4\pi I_o(1-\omega) \text{ and } \frac{4\pi}{3}\frac{dI_o}{d\tau} = F(1-\omega g). \qquad (27) \text{ and } (28)$$

These equations are solved by the application of boundary conditions for the top and bottom of the atmosphere. At the bottom of the atmosphere, $\tau = \tau_1$, the surface albedo is taken to be zero. This corresponds to assuming a dark ocean, and is a good

assumption in this study. The upward flux is thus zero at the bottom of the atmosphere. At the top of the atmosphere, $\tau = 0$, the downward flux is equal to the incident solar flux.

This study will make use of the reflectances measured for clouds in order to retrieve cloud optical properties. The reflectance is the ratio of the upward flux to the incident solar flux at the top of the atmosphere, and is given by

$$R = \frac{(U^2 - 1)(e^{\alpha\tau} - e^{-\alpha\tau})}{(1+U)^2 e^{\alpha\tau} - (1-U)^2 e^{-\alpha\tau}}. \tag{29}$$

The transmittance is the ratio of the downward flux at the bottom of the atmosphere to the incident flux at the top of the atmosphere and is given by

$$T = \frac{4U}{(1+U)^2 e^{\alpha\tau} - (1-U)^2 e^{-\alpha\tau}}, \tag{30}$$

where α and U are given by

$$\alpha = \sqrt{3(1-\omega)(1-\omega g)} \tag{31}$$

$$U = \frac{\alpha}{2(1-\omega)} \tag{32}$$

The above expressions apply when absorption is present. Reflectance and transmittance for a non-absorbing medium, such as water clouds at visible wavelengths, are given by

$$R = \frac{\frac{3}{4}(1-g)\tau}{1+\frac{3}{4}(1-g)\tau} \tag{33}$$

and

$$T = \frac{1}{1 + \frac{3}{4}(1-g)\tau}. \tag{34}$$

These simple relationships provide a way to calculate radiative fluxes at the top and bottom of a vertically uniform cloud from three parameters: optical depth, droplet radius, and the cosine of the solar zenith angle. To treat vertically inhomogeneous clouds, this method is modified to include many layers, each having a reflectance and transmittance that contributes to the reflectance and transmittance for the entire cloud. For this study, the effect of adding layers also allows an inhomogeneous cloud to be modeled by allowing droplet size to grow with each added layer. The total reflectance and transmittance of a multiple layer system is found by considering the simple two-layer model in Fig. 2.1 with incident solar flux $\mu_o F_o$ on the

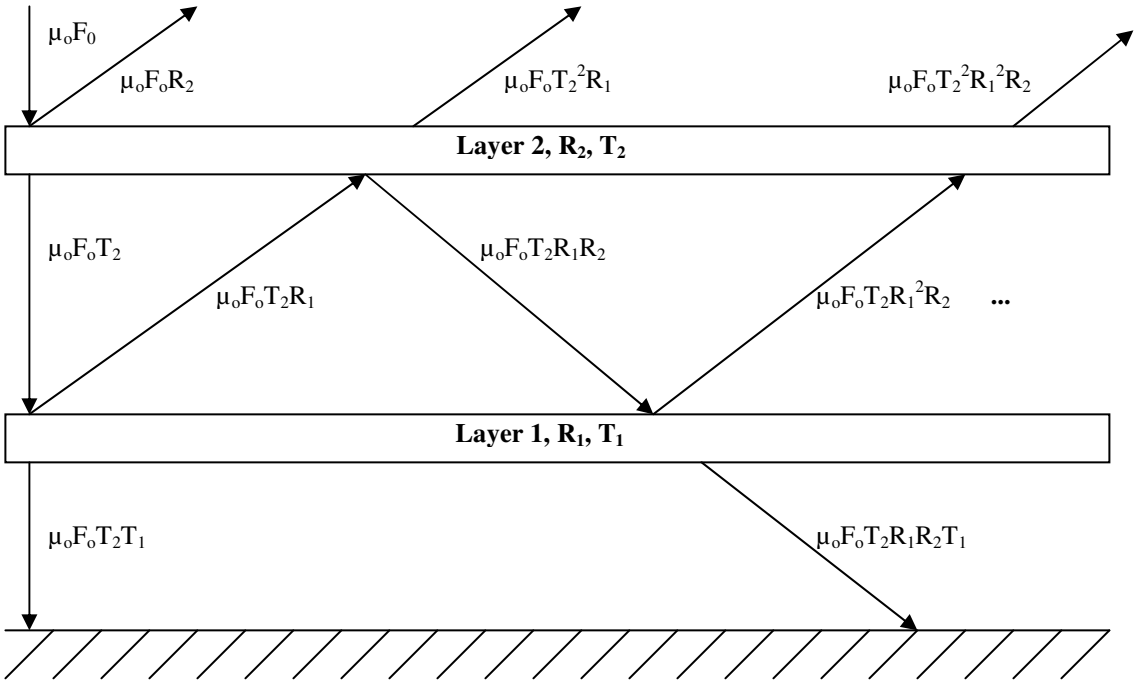

Figure 2.1: Eddington Approximation for adding layers. The system has $\mu_o F_o$ incident on layer 2 and a zero-albedo surface.

top of the atmosphere and a non-reflective surface layer below. Each layer has its own reflectance *R* and transmittance *T*, as illustrated in Figure 2.1. The angles of the solid arrows are for illustrative purposes only as the reflection and transmission occurs in a single column of atmosphere.

While the system illustrated has a surface with an albedo of zero, a nonzero albedo could be easily added by giving the surface a reflectance α_s and a transmittance of zero. Using the equations for upward and downward flux, the total reflectance and transmittance are calculated by summing up all of the individual contributions at the top of atmosphere and the surface. At the top of the atmosphere, reflectance is the fraction of the incident flux F_o that is reflected, or

$$R = \frac{F^+}{\mu_0 F_o} = R_2 + T_2^2 R_1 + T_2^2 R_1^2 R_2 + T_2^2 R_1^3 R_2^2 + T_2^2 R_1^4 R_2^3 + \ldots . \tag{34}$$

Factoring out a $T_2^2 R_1$ beginning with the second term gives

$$R = R_2 + T_2^2 R_1 [1 + R_1 R_2 + R_1^2 R_2^2 + R_1^3 R_2^3 + \ldots] , \tag{35}$$

which is the geometric series $1 + x + x^2 + x^3 + \ldots = 1/(1-x)$. The reflectance of a system with multiple layers is given by

$$R = R_2 + \frac{T_2^2 R_1}{1 - R_1 R_2} . \tag{36}$$

Applying the same method to the downward flux at the surface gives a similar expression for transmittance. The transmittance of a multilayered system is given by

$$T = \frac{T_2 T_1}{1 - R_1 R_2} . \tag{37}$$

The properties of liquid water govern absorption at near infrared and visible wavelengths. Water droplets in the visible spectrum (~0.64 μm) are non-absorbing, while water droplets at 3.7 μm have relatively strong absorption, and hence scatter less. Given two clouds with identical vertically-averaged liquid water content, one homogeneous containing drops of uniform size and the other inhomogeneous with drops growing as altitude increases, the scattering and absorption will be different for the two clouds. The homogeneous cloud has increasing near infrared reflectance for increasing optical depth up to a value at which photons that have not been scattered are absorbed. Once this optical depth has been reached, the cloud is opaque. An adiabatic cloud will have liquid water content growing linearly with height, so if it maintains a constant droplet number concentration with height, it will have more liquid water concentrated at the top of the cloud where drop size is large. It will have relatively little liquid water at cloud base, where drop size is small. For an inhomogeneous cloud, there are two effects at work: reflectance increases as optical depth increases, and reflectance decreases as droplets grow because as droplet size increases, the single scattering albedo decreases, as was shown by the values of the single scattering albedos listed for 3.7 μm in Table 2.1.

CHAPTER 3

RETRIEVAL OF CLOUD PROPERTIES

3.1 ANALYSIS METHODS

The first approach for studying the retrieval issues focused on replacing the vertically uniform clouds on which satellite retrievals are typically based with a vertically non-uniform cloud that accounted for adiabatic cloud development. First, reflectances at 0.64, 1.6, 2.1, and 3.7 μm were calculated using the Eddington Approximation for clouds with a vertically uniform distribution of droplet radii for several combinations of droplet radius and optical depth. The goal was to create reflectance look-up tables for vertically uniform clouds. For vertically uniform clouds, optical depth ranged from 0.1 to 95.1 in 381 steps of 0.25 and droplet radius ranged from 2 to 40 μm in 381 steps of 0.1 μm. The reflectances for the vertically homogeneous clouds were then used to retrieve optical depths and droplet radii based on the 0.64-μm adiabaticvisible reflectance combined with either a 1.6, 2.1, or 3.7-μm adiabatic near infrared reflectance derived for a vertically inhomogeneous cloud that resulted from the adiabatic ascent of moist air. The retrievals were designed to do two things: 1) find the differences in retrieved droplet radii obtained using the three different near infrared wavelengths, and 2) for a cloud growing by adiabatic ascent, find the differences that are expected in retrieved droplet radii when a vertically uniform cloud is assumed.

Reflectances for adiabatic clouds were calculated by specifying the number of layers and layer thicknesses for the cloud. The model cloud for which results are presented used 40 50-m thick layers with an initial cloud base droplet radius of 7 μm and a droplet number concentration of 51 cm^{-3}. The number concentration and initial droplet radius were taken from observational measurements of an unpolluted marine stratus system as described by Brenguier et al. (2003). Each of the 40 layers of the adiabatic cloud was taken to be homogeneous. The reflectance and transmittance calculated for the first layer were identical to those calculated for a homogeneous cloud with the same droplet radius and optical depth. The next layer had a new droplet radius, and the resulting optical depth was given by

$$\tau_{system} = \tau_1 + \tau_2 \tag{38}$$

The cloud reflectances and transmittances were calculated using the Eddington Approximation for multilayered clouds as described in Chapter 2.

The retrieval process involved an iterative search of the reflectances to obtain the droplet radius and optical depth. The procedure is outlined in Figure 3.1. Using the 0.64-μm visible reflectance obtained for an adiabatic cloud and the asymmetry parameter corresponding to an assumed initial droplet radius, the reflectance for a non-absorbing medium as given by the Eddinton Approximation was solved for the optical depth. Optical depth at 3.7 μm was obtained from the visible optical depth as given by

$$\frac{\tau_{3.7\mu m}}{\tau_{0.64\mu m}} = \frac{\sigma_{3.7\mu m}}{\sigma_{0.64\mu m}}, \tag{39}$$

where example values of σ are given in Table 2.1. The near infrared optical depth was then used in conjunction with a range of droplet radii to calculate near infrared

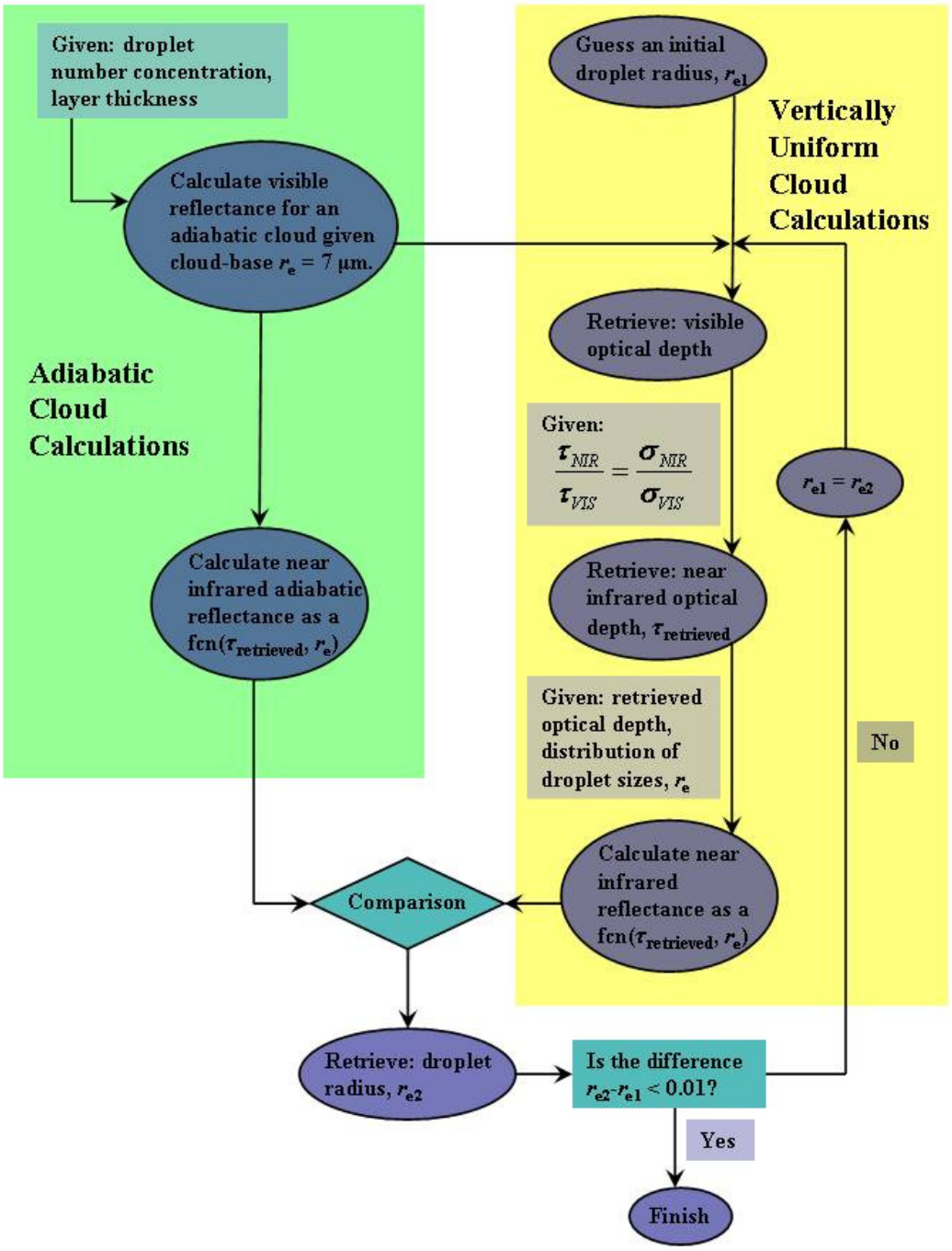

Figure 3.1 Outline of retrieval scheme used to derive r_e and τ from visible and near infrared reflectances.

reflectance as a function of droplet radius. These reflectances were compared to the near infrared reflectance calculated for an adiabatic cloud, and droplet radius at a specific wavelength was retrieved. The retrieved droplet radius became the new initial guess for droplet radius, and the procedure was repeated until the difference between the initial droplet radius and retrieved droplet radius was less than 0.01 μm. In most cases, three or four iterations were sufficient to attain this level of convergence.

3.2 RESULTS

As an aid to understanding the effects of droplet radius growing with altitude within a cloud, Figure 3.2 shows reflectances for homogeneous and adiabatic clouds. Fig. 3.2 a) is 0.64 μm visible reflectance and 1.6-μm near infrared reflectance, b) is 0.64-μm visible reflectance and 2.1-μm near infrared reflectance, and c) is 0.64-μm visible reflectance and 3.7-μm near infrared reflectance. Colored symbols represent reflectances for adiabatic clouds with a cloud-base droplet radius of 7 μm and a droplet number concentration of 51 cm^{-3}. Solid black lines represent reflectances for a homogeneous cloud with a constant radius. Vertical black dotted lines represent reflectances for a vertically homogeneous cloud at constant optical depth. The minimum value of reflectance in Fig. 3.2 is zero, corresponding to a surface with zero albedo. For the vertically uniform clouds, the near infrared reflectances are small when droplet radius is large and relatively large when droplet radius is small and optical depth is large. As expected, reflectances for the adiabatic cloud begin by

following the pattern for the homogeneous clouds with similar droplet radii. For small thicknesses, the adiabatic cloud is close to the corresponding homogeneous cloud. As the cloud thickens, the adiabatic reflectance then crosses over the curves for constant droplet radii toward the smaller reflectances representing larger droplets. As the droplet size increases, absorption increases. Figure 3.2 shows that the visible reflectance is sensitive primarily to changes in optical depth and rather insensitive to droplet radius. The near infrared reflectances, on the other hand, are sensitive mainly to variations in droplet radius for the larger optical depths. Depending on droplet radius, once a certain optical depth is reached, increasing optical depth of a homogeneous cloud has no effect on the near infrared reflectance. The reflectance at near infrared wavelength becomes almost exclusively dependent on droplet radius,

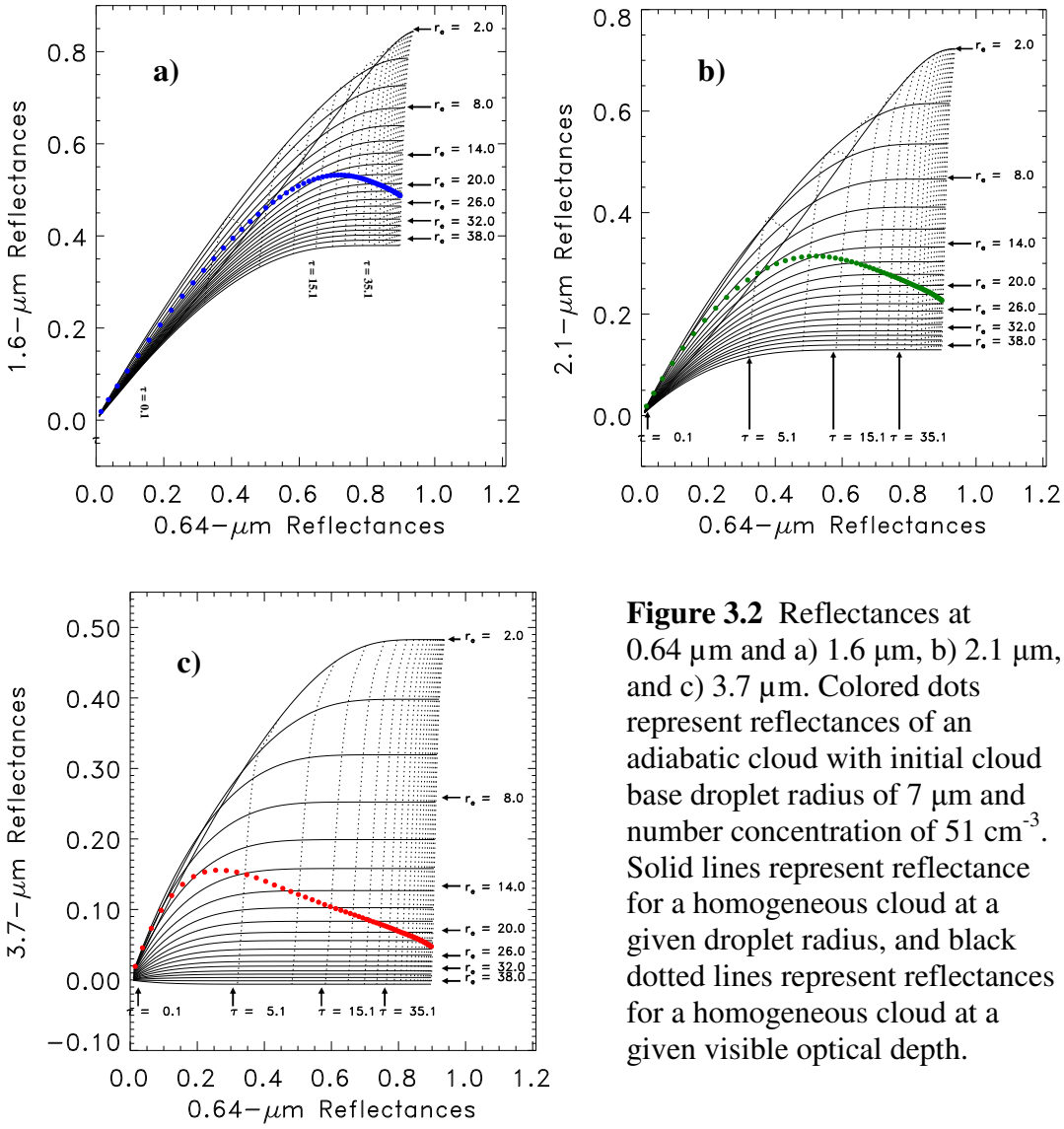

Figure 3.2 Reflectances at 0.64 µm and a) 1.6 µm, b) 2.1 µm, and c) 3.7 µm. Colored dots represent reflectances of an adiabatic cloud with initial cloud base droplet radius of 7 µm and number concentration of 51 cm^{-3}. Solid lines represent reflectance for a homogeneous cloud at a given droplet radius, and black dotted lines represent reflectances for a homogeneous cloud at a given visible optical depth.

which is particularly noticeable at 3.7 µm. Light at 3.7-µm becomes opaque at relatively small optical depths. At such optical depths, no radiation passes through the cloud. It is either reflected or absorbed. The results in the figure suggest that for optically thick clouds, optical depth and droplet radius can be solved for independently of each other using the visible and near infrared reflectances. Due to the greater

penetration depth of light at 1.6 μm, the near infrared reflectance continues to increase to values larger than those for light at 2.1 and 3.7 μm. At 1.6 μm, the cloud does not become opaque until relatively large optical depths.

The relationships between reflectance, optical depth, and droplet radius in Fig. 3.2 allow the occurrence of multiple solutions for droplet radius retrievals. If one follows the lines of constant optical depth from larger to smaller drops, it is possible to have two separate droplet radii at a given optical depth producing the same reflectances. This feature is particularly prominent for smaller droplet radii at small τ. Multiple solutions are most pronounced for the 0.64 and 1.6-μm reflectances shown in Fig. 3.2a. For these wavelengths, the lines of constant optical depth show a more distinct curve throughout the cloud, suggesting that multiple solutions for droplet radius at a given pair of 0.64 and 1.6-μm reflectances can exist for many combinations of optical depth and droplet radius. In order to deal with this issue, the iterative scheme developed to retrieve droplet radius and optical depth calculated extensive look-up tables. Reflectances calculated for vertically uniform clouds used droplet radii incremented every tenth of a micron and optical depth incremented by 0.25.

Figure 3.3 shows the droplet radius vertical profile for a 2000-meter thick cloud with cloud base droplet radius of 7 μm and number concentration of 51 cm^{-3}. For thick clouds generated by the adiabatic ascent of moist air, droplet radius grows as $H^{1/3}$.

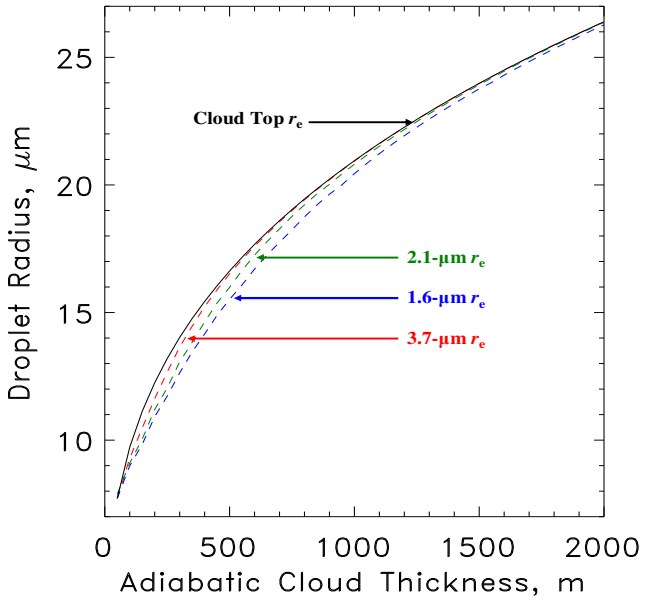

Figure 3.3 Vertical profiles of droplet radius. The solid line is droplet growth in an adiabatic cloud, and the three dashed lines are the retrieved droplet radii for vertically homogeneous clouds for the given thickness. Red is the profile obtained for the 3.7-μm reflectance, green is the 2.1-μm reflectance, and blue is the 1.6-μm reflectance.

The first cloud layer at 50 m in Figure 3.3 is homogeneous, and as expected, the droplet radii retrieved at all three near infrared wavelengths matched the cloud top droplet radius for this first layer. After a second layer was added, droplet radius was no longer constant throughout the cloud, and the three droplet radii retrieved for a homogeneous cloud using the 1.6, 2.1, and 3.7-μm reflectances began to diverge slightly from the adiabatic cloud top droplet radius. The penetration depth, the depth from which reflected photons leave the cloud, is shortest at 3.7 μm. Consequently, the retrieved droplet radius at 3.7 μm was only slightly smaller than the adiabatic cloud top radius. Light at 2.1 μm penetrates a bit further into the cloud, and hence an even smaller droplet radius was retrieved. Light at 1.6 μm penetrates the furthest into the cloud, and the retrieved droplet radius was the smallest, more representative of droplet radii at a lower level in the cloud. According to Fig. 3.3 light at different wavelengths is extinguished at different cloud depths. Light at 3.7 μm was saturated by about 600 or 700 m, where photons have penetrated into the cloud as far as they can, and the

retrieved radius begins to approach the cloud top value. The cloud is almost completely opaque at 3.7 μm for this thickness. For 2.1 μm, saturation occurred at about 1500 m, and for 1.6 μm, saturation occurred at depths greater than 2000 m. MODIS retrievals are expected to show that droplet radii retrieved using 3.7-μm reflectances are largest, followed by droplet radii retrieved using 2.1-μm reflectances and droplet radii retrieved using 1.6-μm reflectances. For optically thick marine stratus, Hayes et al. (2009) obtained a progression in retrieved radii similar to that shown in Fig. 3.3. MODIS retrievals for overcast pixels that were not optically thick, however, produced 2.1-μm derived r_e > 1.6-μm derived r_e > 3.7-μm derived r_e. The results presented in Fig. 3.3 do not match the MODIS observations for optically thin or partly cloudy regions. Additionally, the presence of the large droplet radii retrieved using the MODIS 2.1-μm reflectances are rarely, if ever, reported in aircraft measurements, although recent observations obtained during VAMOS Ocean-Cloud-Atmosphere-Land Study Regional Experiment (VOCALS) may report such large droplets (Twohy, private communication).

Figure 3.4 shows retrieved optical depths and the adiabatic optical depths over the same 2000 m range of cloud thickness. As expected, the optical depths from the adiabatic model and those retrieved using 1.6, 2.1, and 3.7-μm reflectances were nearly identical because optical depth is derived primarily from the visible reflectance and the asymmetry parameter, *g*, is only a very weak function of droplet radius, as shown in Table 2.1. From Figure 3.3, the maximum difference between adiabatic cloud top droplet radius and retrieved radius was on the order of 1 μm, a departure

present at small optical depths up until approximately $\tau = 40$. As indicated by Table 2.1 the asymmetry parameter is the same within two significant figures for two droplets differing by only 1 μm.

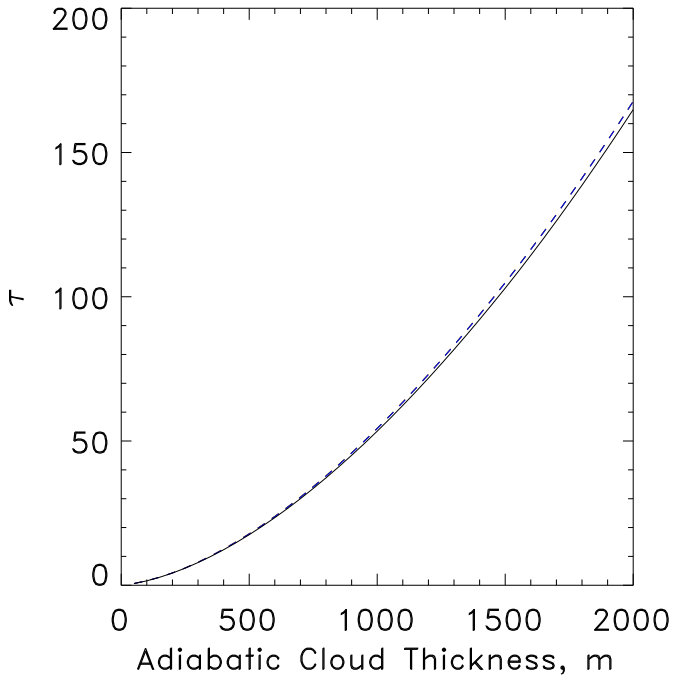

Figure 3.4 Total visible optical depth (solid black line) and retrieved optical depth for adiabatic clouds (dashed lines). The optical depths were obtained using the 1.6, 2.1, and 3.7-μm reflectances to retrieve the droplet radius. The visible optical depths obtained separately with each of the three near infrared wavelengths were identical.

Figure 3.5 shows $ln\ (\tau/\tau_o)$ and $ln\ (r_e/r_{eo})$, where τ and r_e are the optical depth and droplet radius up through a given cloud layer and τ_o and r_{eo} are the optical depth and droplet radius for the layer at the bottom of the cloud. The slope for the adiabatic cloud (black line), given by $d \ln r_e / d \ln \tau$, was constant and approximately equal to 0.205, which is close to the value of 0.2 derived in chapter 2 for thick adiabatic clouds. The slope was not expected to be exactly 0.2 owing to the effects of the finite droplet number concentration at cloud base and the discrete homogeneous layers used in the model. When the cloud was optically thin, the results in Fig. 3.5 for $ln\ (\tau/\tau_o) < 1$

showed that the retrieved cloud properties were extremely sensitive to the chosen initial cloud base number concentration and droplet radius. As the cloud thickened, the slopes $d\ ln\ r_e/d\ ln\ \tau$ derived for the three wavelengths used to retrieve the droplet radius began to approach 0.2. Fig. 3.5 also shows that when vertically uniform clouds are assumed, the $d \ln r_e / d \ln \tau$ derived from the retrieved properties were not constant. The retrievals at the near infrared wavelengths gave values greater than 0.2 at approximately $ln\ (\tau/\tau_o) = 1.5$, and converged to the adiabatic value as optical depth increased. The 3.7-µm $d \ln r_e / d \ln \tau$ most closely resembled the adiabatic value, and

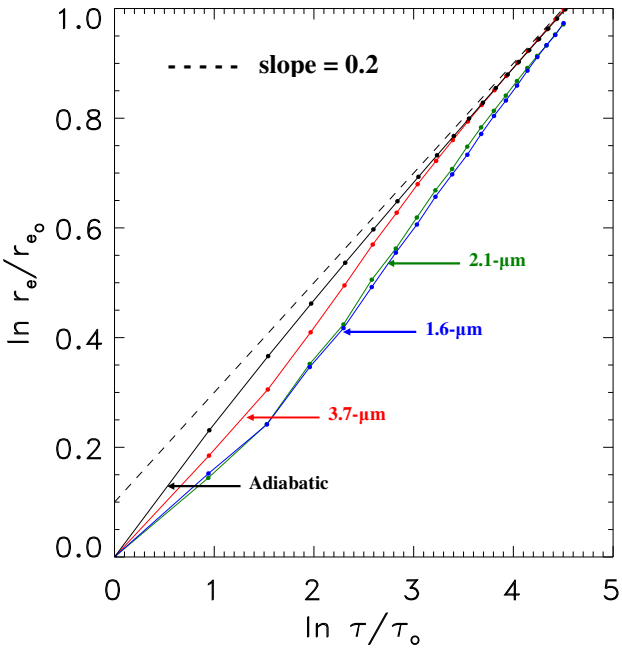

Figure 3.5 $ln\ \tau/\tau_0$ and $ln\ r_e/r_{eo}$ for an adiabatic cloud(black line), 3.7-µm derived droplet radius (red line), 2.1-µm derived droplet radius(green line), and 1.6-µm derived droplet radius(blue line). τ and r_e represent the optical depth and droplet radius of a given height for the retrieved $d \ln r_e / d \ln \tau$ using the three near infrared wavelengths. τ_o and r_{eo} represent the optical depth and droplet radius at the bottom of the cloud. For the adiabatic cloud, τ and r_e represent total optical depth and cloud-top droplet radius.

converged to it by approximately $ln\ \tau/\tau_o = 3$. The departure from the adiabatic relationship was most severe when using 1.6-µm reflectances to retrieve droplet radius, which produced the largest overestimate, especially when the cloud was

optically thin. As is described in the next chapter neither the progression of retrieved droplet radii with near infrared wavelength nor the values of $d \ln r_e / d \ln \tau$ were found in the retrievals of cloud properties from MODIS observations. Figure 3.5 indicates that the slopes at all three wavelengths should be greater than 0.2. While the treatment of clouds as vertically uniform in satellite retrievals may produce some error in retrieved cloud properties, accounting for the profile of droplet radius will not explain the cloud properties retrieved using the MODIS reflectances, provided of course, the clouds being observed behave as adiabatic clouds.

CHAPTER 4

EFFECTS OF HORIZONTAL VARIABILITY IN CLOUD PROPERTIES

4.1 ANALYSIS METHODS

Based on the simulations described in the previous chapter, the retrievals for the horizontally homogeneous cloud would produce a progression of retrieved droplet radii for the MODIS near infrared reflectances that yielded larger radii at the longer wavelengths, the progression expected given the growth of droplet radius with altitude in adiabatic clouds. The results fail to explain why larger droplet radii are often retrieved when using 2.1 and 1.6-μm reflectances than when using 3.7-μm reflectances. According to Barker (1996), a spatially inhomogeneous cloud with a given mean optical depth has different radiative properties than a horizontally uniform

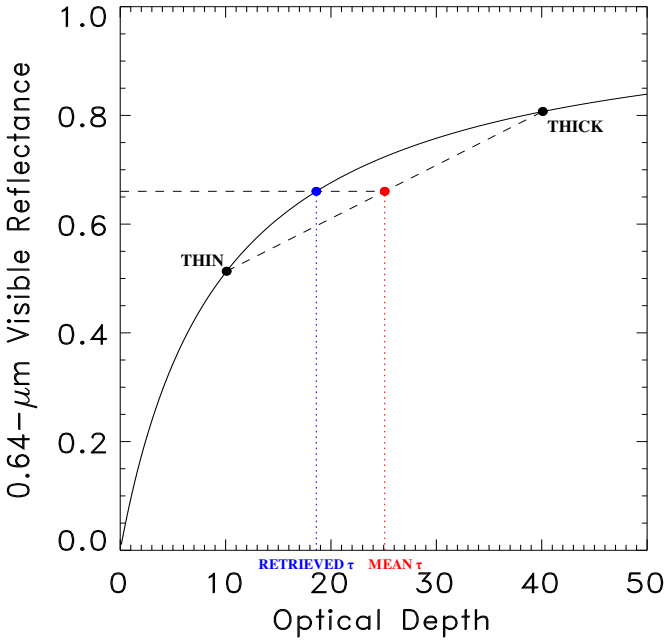

Figure 4.1 Optical depth and visible reflectance for a cloud with equal portions of optically thin and optically thick cloud within an imager pixel.

cloud. The differences arise because the reflectances depend nonlinearly on the cloud properties. The dependence of visible reflectance on optical depth is shown in Fig. 4.1. For a cloud containing equal amounts of optically thin and optically thick areas, the average reflectance bisects a straight-line between the two optical depths in Fig. 4.1. The optical depth retrieved given the mean reflectance for the pixel will underestimate the mean optical depth for the pixel.

Hayes et al. (2009) found that overcast 1-km MODIS pixels in regions containing both partly-cloudy and cloud-free areas had smaller optical depths than overcast pixels that were in regions completely covered by low-level marine stratus. If each pixel had a horizontal distribution of optical depths, ranging from very thin, semitransparent regions to opaque, thick clouds, an underestimate in the mean optical depth would be expected. If the pixel was only partially covered with clouds, or if the cloud was semitransparent, the reflectances measured at visible and near infrared wavelengths would be smaller than if the entire pixel was overcast and optically thick. According to Fig. 4.2, smaller visible reflectance leads to a smaller optical depth. Using the underestimate of the optical depth and the smaller measured near infrared reflectance to retrieve droplet radius causes an overestimation of the droplet radius. Figure 4.2 shows visible and near infrared reflectances for selected optical depths and droplet radii, and illustrates the nonlinear relationships between cloud properties and the reflectances that cause biases in retrieved droplet radius and optical depth when there are horizontal variations in optical depth. Consider a portion within a pixel with an optical depth of 10.1 and droplet radius of 14 μm and an optically thin portion with

an optical depth of 1.1 and a droplet radius of 6 µm. These two portions are represented by the black dots in Fig. 4.2. The average optical depth of the two pixels is 5.6, the average droplet radius is 10 µm, shown in red. When retrievals are performed using the average 0.64 and 2.1-µm reflectances, however, the retrieved optical depth is 4.48, and the retrieved droplet radius at this optical depth is 15.9 µm, which is an underestimate of optical depth and an overestimate of droplet radius, as shown by the blue dot in Fig. 4.2.

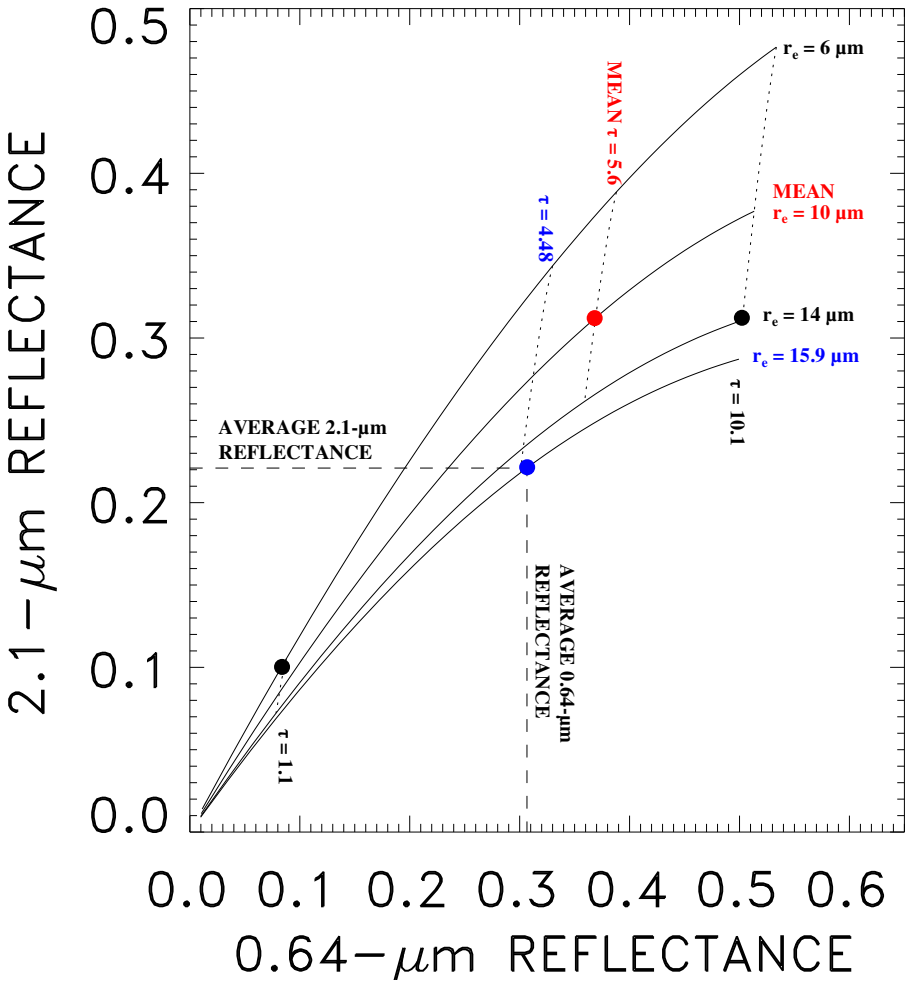

Figure 4.2 0.64-µm and 3.7-µm reflectances for selected optical depths and droplet radii. When visible and near infrared reflectances are underestimated, a smaller optical depth and larger droplet radius are retrieved.

The overestimation of droplet radius is likely to be most severe when using the 1.6 and 2.1-μm MODIS reflectances to retrieve droplet radius because the absorption by liquid water at 3.7 μm is greater than the absorption by liquid water at the shorter wavelengths. Reflected photons at 1.6 μm have a larger penetration depth, and so the effect of optically thin portions of the cloud would be more apparent in the droplet radii retrieved using 1.6-μm reflectances.

To examine the effects of spatial variability, the model described in Chapter 3 to account for the impacts of vertical inhomogeneity was adapted to account for subpixel-scale variation in optical depth as well. The Independent Pixel Approximation (IPA) was used in calculating the radiative properties for the pixel and subpixels (Cahalan 1994). In the IPA, the regional mean cloud albedo is obtained by partitioning the cloud into subregions, computing an albedo for each subregion, and then averaging all subregion albedos. Cahalan (1994) showed that the IPA provided reasonably accurate estimates of mean solar fluxes transmitted by marine stratus clouds.

MODIS observations were used to derive a realistic distribution of pixel-scale optical depths. The data was composed of 200 50-km scale regions overcast by marine stratus between 20º N and 50º N drawn from orbital passes over the Northwestern Atlantic. A region was considered roughly "overcast" for the purposes of this simulation when it contained fractional cloud cover greater than 0.8. Each selected region had to have at least 10% of the pixels overcast by marine stratus as deduced from partly cloudy pixel retrievals (Coakley et al. 2005). Methods described

by Matheson et al. (2005) were used to insure that the regions contained no clouds other than a single layer of marine stratocumulus. Thirty pixels overcast by marine stratocumulus were chosen randomly from each region under the constraint that no two pixels used were closer than 3 km from one another in order to reduce spatial correlations among neighboring pixels. The MODIS pixel-scale optical depths were used to constrain the average for the subpixel distribution of optical depths. A gamma distribution, defined by mean and variance, was used to estimate the subpixel distribution of optical depth for marine stratocumulus (Barker 1996, Kato et al. 2006). A gamma distribution was randomly sampled to generate 20 cells around the pixel-scale mean optical depth with the variance prescribed by Kato et al. (2006) based on large eddy simulations (LES) of marine stratocumulus.

Using the optical depths randomly generated within each pixel, a corresponding distribution of droplet radius and adiabatic cloud thickness was calculated from (6) and (11). Visible and near infrared reflectances were then calculated for each cell within the pixel by allowing the cloud to grow adiabatically so that it attained the prescribed pixel-scale mean optical depth. Retrievals of the properties based on spatially uniform clouds were performed for each subpixel to obtain droplet radius and optical depth. As was noted in the previous chapter, the retrieved values differed little from the cloud-top radius and optical depths for adiabatic clouds. Mean values of the droplet radii and optical depths retrieved for the subpixels along with the corresponding mean reflectances were determined for the entire pixel. The averaged properties for the subpixels were compared to the

properties retrieved for the pixels using average reflectances to assess the impact subpixel-scale variability on cloud property retrievals.

4.2 RESULTS

Regions were selected that had cloud cover greater than 0.8 as derived from the partly cloudy pixel retrievals. The pixel-scale distribution of retrieved optical depths is shown in Fig. 4.3 by the solid line. The mean optical depth was

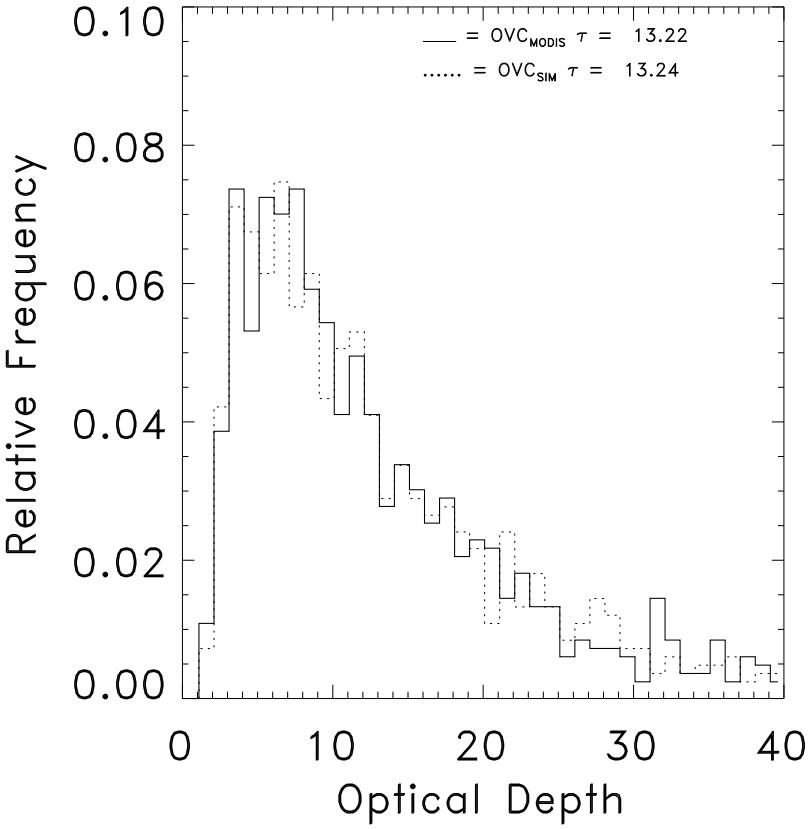

Figure 4.3 MODIS pixel-scale optical depth (solid line) and simulated pixel-scale distribution of optical depths (dotted line). The MODIS optical depths were obtained from 200 50-km scale regions with fractional cloud cover greater than 0.8. Thirty overcast pixels were drawn at random from each region. The average optical depths of the observations and simulations are also given.

13.22, which is close to the value found by Hayes et al. (2009) of 14.11 for independent observations of marine stratus drawn from overcast 50-km scale regions. The pixel-scale optical depth distribution generated in the simulation, the dotted line in Fig. 4.3, agreed with the pixel-scale distribution of optical depths, as it should.

The droplet radii derived using the three near infrared MODIS reflectances are shown in Figure 4.4. Figure 4.4 illustrates the problem discussed in Chapter 1. For pixels overcast by adiabatic clouds, droplet radius should increase when retrieved

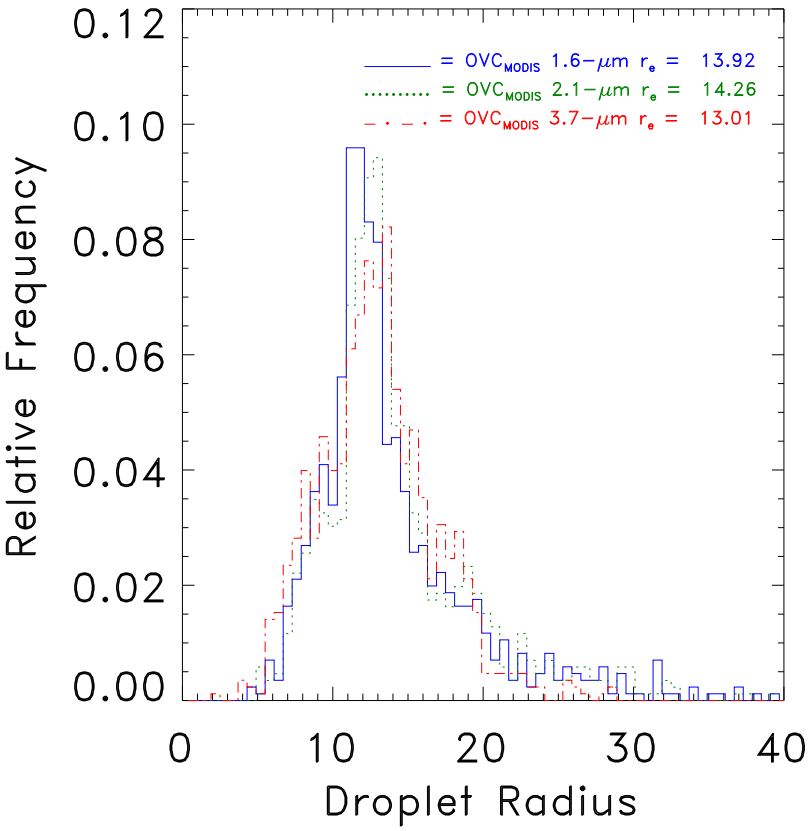

Figure 4.4 MODIS pixel-scale droplet radii retrieved using 1.6 μm (blue solid line), 2.1 μm (green dotted line) and 3.7 μm (red dash-dotted line) reflectances. The pixel-scale averages are given for the retrieved droplet radii.

using the longer wavelengths. For the MODIS observations, the largest radius was retrieved using 2.1-μm reflectances, and the smallest was retrieved when using the 3.7-μm reflectances. Adding a subpixel-scale distribution of optical depth is likely to alter the above droplet radius distribution because introducing variability in optical depth within the pixel leads to smaller reflectances and thus larger retrieved droplet radii. The expectation is that droplet radii at all three wavelengths will be larger, but the retrieved droplet radii using the 1.6 and 2.1-μm reflectances will be larger than that retrieved using the 3.7-μm reflectance. Since water absorbs more strongly at 3.7 μm, the effect of subpixel scale variability will be diminished because a larger percentage of clouds will be opaque at this wavelength. Figure 4.5 shows droplet radii from the simulations and from MODIS retrievals using the 1.6, 2.1, and 3.7-μm reflectances. For the vertically inhomogeneous, horizontally uniform simulations in Chapter 3, the large droplet radii retrieved using the 1.6-μm and 2.1-μm reflectances could not be simulated. The results of those simulations also suggested that droplet radius retrieved using 3.7-μm reflectances should be greater than that retrieved using 2.1-μm reflectances, which should be greater than that retrieved using 1.6-μm reflectances. When horizontal variability was added to the simulation, however, the resulting mean droplet radii retrieved for the subpixels were all greater than the droplet radii retrieved using the MODIS observations. The largest droplet radii were retrieved using 1.6-μm reflectances, which was expected since subpixel-scale variability most strongly affects retrievals performed at the wavelengths with the least absorption by liquid water.

The simulation started with a cloud base droplet radius of 5 μm and droplet number concentration of 51 cm^{-3} for each subpixel. Adiabatic ascent was performed until the prescribed optical depth was reached. Within a 1-km pixel, a uniform distribution of cloud base droplet radius and number concentration is unlikely. Nonetheless, even when working under this assumption, the simulation produced

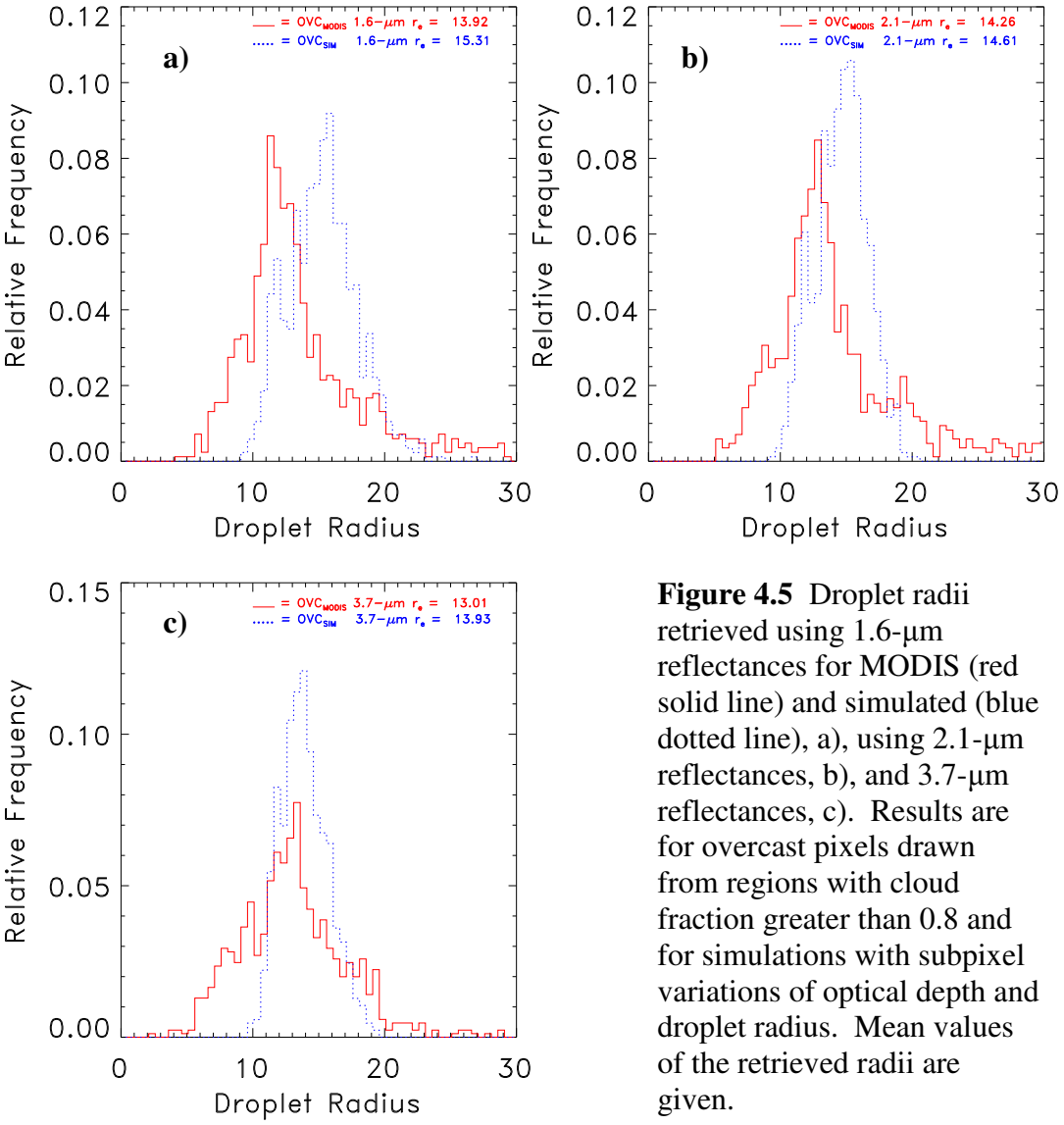

Figure 4.5 Droplet radii retrieved using 1.6-μm reflectances for MODIS (red solid line) and simulated (blue dotted line), a), using 2.1-μm reflectances, b), and 3.7-μm reflectances, c). Results are for overcast pixels drawn from regions with cloud fraction greater than 0.8 and for simulations with subpixel variations of optical depth and droplet radius. Mean values of the retrieved radii are given.

distributions of droplet radii that came close to resembling the observed MODIS pixel-scale distributions. Adding subpixel variability to the droplet radii and number concentrations at cloud base could improve the agreement.

The slope, $d \ln r_e / d \ln \tau$, were also calculated for both the MODIS observations and the simulations. The MODIS slopes based on the droplet radii retrieved using the three near infrared reflectances are shown in Figure 4.6. With the

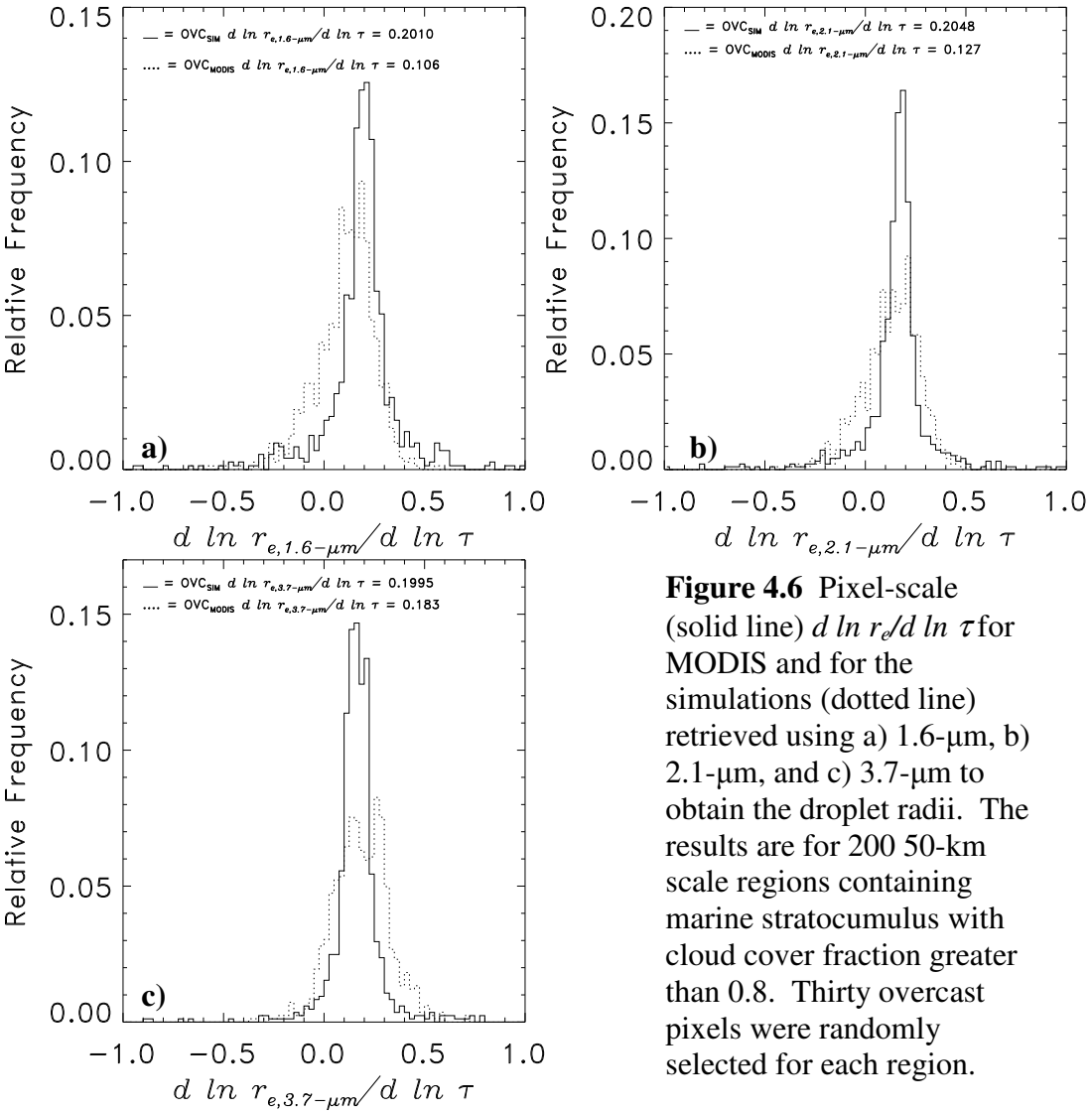

Figure 4.6 Pixel-scale (solid line) $d \ln r_e / d \ln \tau$ for MODIS and for the simulations (dotted line) retrieved using a) 1.6-μm, b) 2.1-μm, and c) 3.7-μm to obtain the droplet radii. The results are for 200 50-km scale regions containing marine stratocumulus with cloud cover fraction greater than 0.8. Thirty overcast pixels were randomly selected for each region.

subpixel variations, the slopes obtained with the simulations were consistent with those expected for adiabatic ascent. Interestingly, the simulated slopes exhibited a distribution of values with means near the expected value, $d \ln r_e / d \ln \tau \approx 0.2$. The slopes were also in closer conformity with the MODIS observations than the slopes retrieved for spatially uniform simulations in Chapter 3, for which $d \ln r_e / d \ln \tau$ for droplet radii retrieved using all three near infrared reflectances were greater than 0.2. The slopes calculated in the simulation were also close to those obtained by Hayes et al. (2009) for optically thick clouds drawn from 50-km scale regions overcast by marine stratus. As mentioned earlier, this simulation was performed on the assumption that cloud base droplet number concentration and droplet radius were spatially uniform. If distributions of these properties were added, the simulated slopes and retrieved droplet radii might resemble those derived from MODIS more closely.

For the MODIS observations, the partly cloudy pixel retrievals were separated into groups based on pixel scene identification: pixels identified as overcast by clouds in a single-layered system, and pixels initially identified as partly cloudy but for which the retrieved cloud fraction was 1.0 The two types of overcast pixels and how they are identified are described by Coakley et al. (2005). Fig. 4.7 shows optical depths for pixels identified as overcast (dotted) and partly cloudy pixels initially identified as partly cloudy but for which the retrieved cloud cover was 1.0 (solid). The pixels initially identified as partly cloudy had a lower mean pixel-scale optical depth of 10.59 than the pixels identified as overcast, which had a mean optical depth of 15.69. As

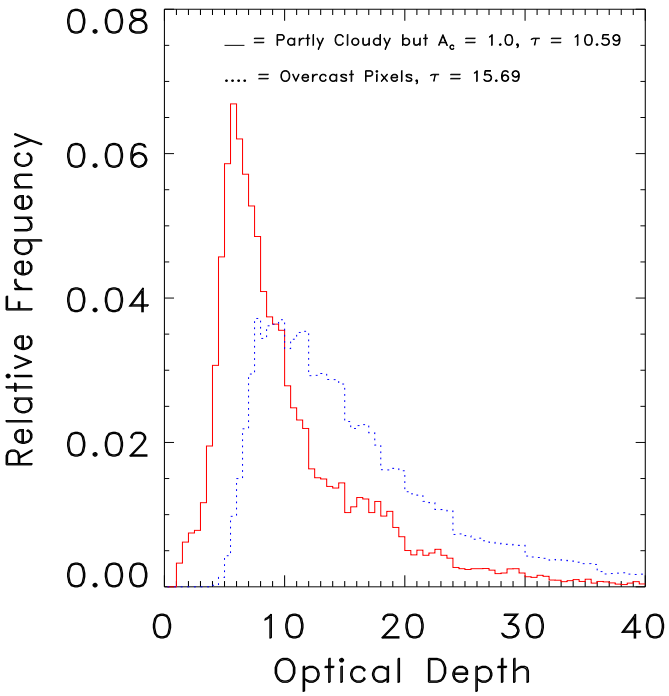

Figure 4.7 Optical depth for pixels identified as overcast (dotted) and pixels initially identified as partly cloudy but for which the retrieved cloud cover was 1.0 (solid) in the partly cloudy pixel retrieval scheme.

indicated earlier in the chapter, a pixel with a smaller optical depth may be more susceptible to the effects of subpixel variability, leading to large values for the retrieved droplet radii. Given this information, the pixels initially identified as partly cloudy were expected to have larger droplet radii than those identified as overcast. Fig. 4.8 shows retrieved droplet radius using a)1.6-μm reflectances, b) 2.1-μm reflectances, and c) 3.7-μm reflectances for pixels initially identified as partly cloudy (solid) and pixels initially identified as overcast (dotted). The droplets for the pixels initially identified as partly cloudy were on average about 1 μm larger than those for the pixels identified as overcast when using the 1.6-μm reflectance to retrieve droplet radius, consistent with the differences between horizontally uniform and horizontally non-uniform simulations. In this case, the effects of partly cloudy pixels on retrieved droplet radii were similar to the effects of horizontal inhomogeneity. When 3.7-μm reflectance was used to retrieve the droplet radius, the difference between the partly

cloudy pixels and the overcast pixels decreased. Since photons at 1.6-μm have a greater penetration depth than photons at 3.7 μm, the photon leakage at 1.6 μm as a result of broken clouds would be greater.

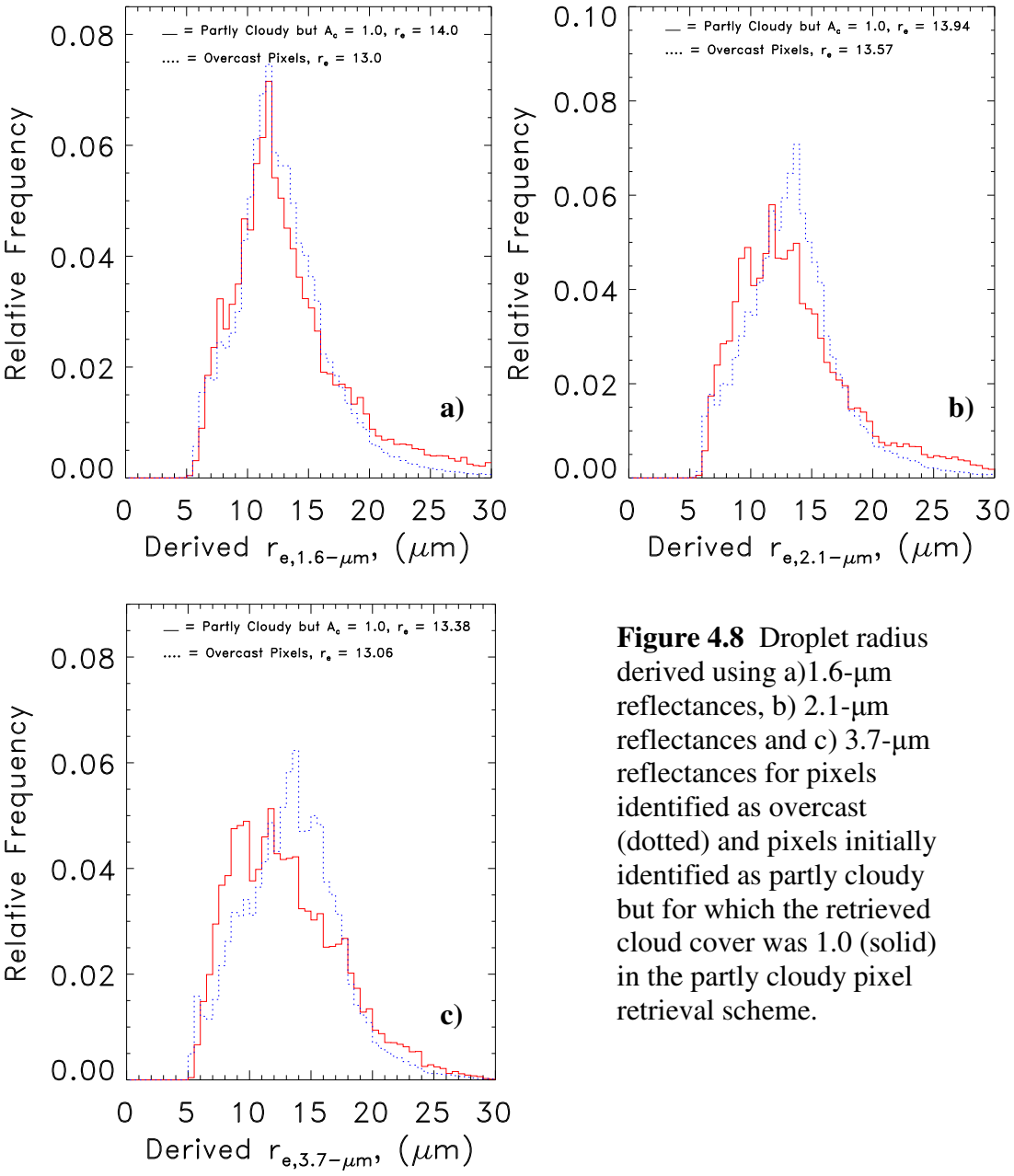

Figure 4.8 Droplet radius derived using a)1.6-μm reflectances, b) 2.1-μm reflectances and c) 3.7-μm reflectances for pixels identified as overcast (dotted) and pixels initially identified as partly cloudy but for which the retrieved cloud cover was 1.0 (solid) in the partly cloudy pixel retrieval scheme.

CHAPTER 5

PROPERTIES OF MARINE STRATOCUMULUS RETRIEVED FROM MODIS 500-m IMAGERY

The results in Chapter 4 indicated that variable optical depth within pixels was at least partially responsible for the biases observed in MODIS cloud property retrievals at the 1-km scale. As a next step, retrievals of droplet radius and optical depth from higher spatial resolution MODIS data were performed. Visible optical depth and droplet radius retrieved using 0.64, 1.6 and 2.1-μm reflectances were obtained from MODIS observations at the 500-m scale. The 500-m observations do not retrieve droplet radius using 3.7-μm, so obtaining data at this wavelength was not possible. These 500-m pixels were aggregated into a 2-km pixel, and the cloud properties obtained by averaging the properties for the sixteen 500-m pixels were compared to the properties retrieved using the average reflectances of the 2-km pixel. This particular method is analogous to the simulation undertaken in Chapter 4, with the 500-m retrievals representing the different subpixels within each 1-km pixel in Chapter 4, and the properties retrieved from average radiances representing the MODIS 1-km retrievals in Chapter 4. Using the 500-m observations can help to further explore the role of spatial heterogeneity and provide observational evidence for the findings of Chapter 4.

The data were separated into two categories: one group consisting of overcast regions with average fractional cloud cover greater than 0.95, and another group

consisting of broken-cloud regions with average fractional cloud cover between 0.6 and 0.8. The cloud cover was deduced using the partly cloudy pixel retrievals applied to 1-km MODIS imagery. Previous work indicated that retrieved cloud properties from regions with partial cloud cover exhibited a greater bias than occurred for regions that were overcast. By separating the regions into two groups for this analysis, the effect of subpixel variation of cloud parameters was documented both for regions that were nearly overcast and for regions that contained broken clouds. The biases were expected to be larger within the broken-cloud regions. Additionally, the data were separated into pixels identified as overcast by the MODIS cloud processing scheme and those identified as overcast by the Partly Cloudy Pixel Retrievals (PCPR) to assess whether the biases obtained with the MODIS identifications were avoided by using the partly cloudy pixel retrievals. The primary difference between the two retrieval schemes is in their treatment of the pixel-scale cloud cover. The MODIS cloud processing scheme classifies a pixel as overcast if it contains clouds, and cloud-free if no clouds are detected (Platnick et al. 2003). The MODIS 500-m pixel identification is the aggregation of the identification at the 250-m scale, the resolution at which the identification is actually performed. At the 2-km resolution, Coakley et al. (2005) found that most pixels containing marine stratocumulus would be classified as either overcast or cloud-free by threshold detection schemes like that used in the MODIS identifications, even though approximately 40% of the cloudy pixels contained broken clouds. The partly cloudy pixel retrieval method was developed to retrieve cloud properties from fields of view that had only partial cloud cover. It is

strictly applicable to single-layered cloud systems such as the marine stratocumulus examined in this thesis. The retrieval scheme identifies pixels as either cloud-free, overcast by thick clouds, partly cloudy, or pixels initially identified as partly cloudy, but upon retrieval of the cloud properties are found to be overcast. Since the partly cloudy pixel retrieval scheme accounts for partial cloud cover, the number of PCPR overcast pixels will be smaller than the number of overcast pixels identified by the MODIS scheme. Once the overcast pixels were identified by both schemes cloud properties were retrieved using the partly cloudy pixel retrieval scheme with the assumption that the pixels were overcast.

5.1 CASE STUDIES

Three 50-km scale regions were chosen to represent three common cloud systems: a nearly overcast region, a typical region with a mix of overcast and partly cloudy pixels, and a broken-cloud region with mostly partly cloudy pixels. For each region, the differences in retrieved optical depth and droplet radius retrieved using 1.6 and 2.1-μm reflectances were explored for the MODIS and PCPR overcast pixel identifications. The results show the differences in the retrieved properties obtained with the two identification schemes for varying amounts of cloud cover.

5.1.1 Typical Scene with Overcast and Partly Cloudy Pixels

The region selected contained roughly equal numbers of overcast and partly cloudy pixels as shown in Figure 5.1. It was observed on 17 May, 2004 at 1143 UTC, and located at 41.72º N, 20.3º W. The satellite zenith angle was 51.6º, the solar zenith angle was 30.01º, and the azimuth angle was 164.2º. The regional mean cloud cover for this scene was 0.9. The cloud cover was determined using the partly cloudy pixel retrievals applied to 1-km MODIS pixels. Fig. 5.1 shows 0.64-μm reflectivity at a) 500-m resolution and b) 2-km resolution. Light shades of gray indicate high 0.64-μm visible reflectivity, and hence larger optical depths. Darker gray areas are thin clouds and black areas are broken clouds or cloud-free. One 2-km pixel is made up of 16 500-m pixels. The difference between the two spatial resolutions is apparent. Within just one 2-km pixel in Fig. 5.1, visible reflectivity is highly variable among the associated 500-m pixels, indicating that the 2-km pixel contains a range of cloud thicknesses that are resolved at the higher spatial resolution. Fig. 5.1 c) shows the 11-μm radiance and 0.64-μm reflectivity for this scene at the 2-km pixel resolution. The pixels classified as overcast by the partly cloudy pixel retrieval scheme are in red. These pixels were also classified as overcast by the MODIS cloud mask. The additional pixels classified as overcast by MODIS are in blue. The PCPR overcast pixels were concentrated in the most optically thick parts of the cloud. Because clouds were detected, MODIS also identified pixels in the more optically thin regime as overcast. In Fig. 5.1 c), these pixels are numerous.

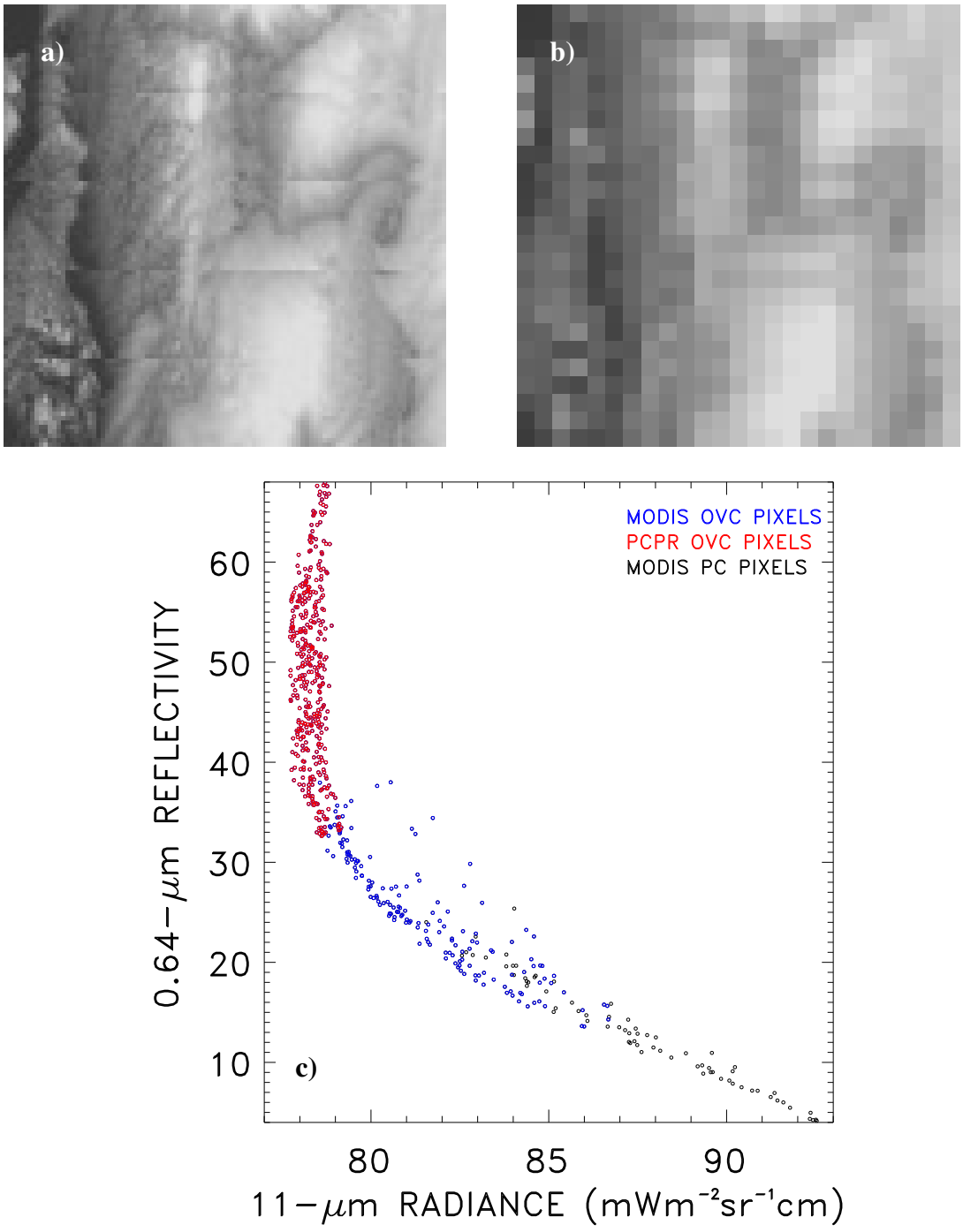

Figure 5.1 Images constructed from Terra MODIS 0.64-µm reflectivity at a) 2-km resolution and b) 500-m resolution, and c) 11-µm radiance and 0.64-µm reflectivity at the 2-km scale. Red dots indicate pixels identified as overcast by the partly cloudy pixel retrievals. Blue dots indicate pixels identified as overcast by the MODIS cloud mask. Black dots indicate pixels identified by the MODIS cloud mask as being partly cloudy.

The inclusion of pixels with only partial cloud cover in the MODIS overcast pixel identifications was expected to produce larger biases in retrieved optical depth and droplet radius than those obtained with the PCPR. The bias is the difference given by the droplet radii and optical depths retrieved using the average reflectances for the 2-km pixels minus the average of the retrieved properties for the associated 500-m pixels. In this thesis, the bias for each cloud property will be described by the terms 1.6-μm Δr_e, 2.1-μm Δr_e, and $\Delta\tau$. Retrieved droplet radii using average reflectances were expected to be larger than the average of the droplet radii for the associated 500-m pixels as discussed in Chapter 4. Likewise, optical depths retrieved using the average reflectances were expected to be smaller than the average of the optical depths retrieved for the associated 500-m pixels.

Fig. 5.2 shows a) 1.6-μm Δr_e, b) 2.1-μm Δr_e, and c) $\Delta\tau$ as functions of the average cloud optical depth. Red dots are pixels classified as overcast by the PCPR scheme and blue dots are the additional pixels classified as overcast by the MODIS scheme. For the 1.6 and 2.1-μm Δr_e, the biases for both retrieval schemes are most prominent for the optically thin clouds. Pixels with these low average optical depths may lead to more biased retrievals due to the effects of broken clouds and spatial heterogeneity. At high optical depths, the Δr_e at both 1.6 and 2.1 μm approaches zero. For thick clouds, the reflectances at the near infrared wavelengths are no longer affected by variations in cloud thickness, thereby reducing the variability in reflectances that lead to biases in the retrieved droplet radii. It is also possible that as clouds thicken, variations in droplet radii within the 2-km scale become smaller. For

the 1.6-μm reflectances, the MODIS overcast pixel identification led to droplet radii that were 0.138 μm larger than the average for the 2-km pixel. In the case of the partly cloudy pixel retrievals the droplet radii were 0.085 μm larger. For 2.1-μm reflectances, the MODIS identification led to droplet radii that were 0.091 μm larger,

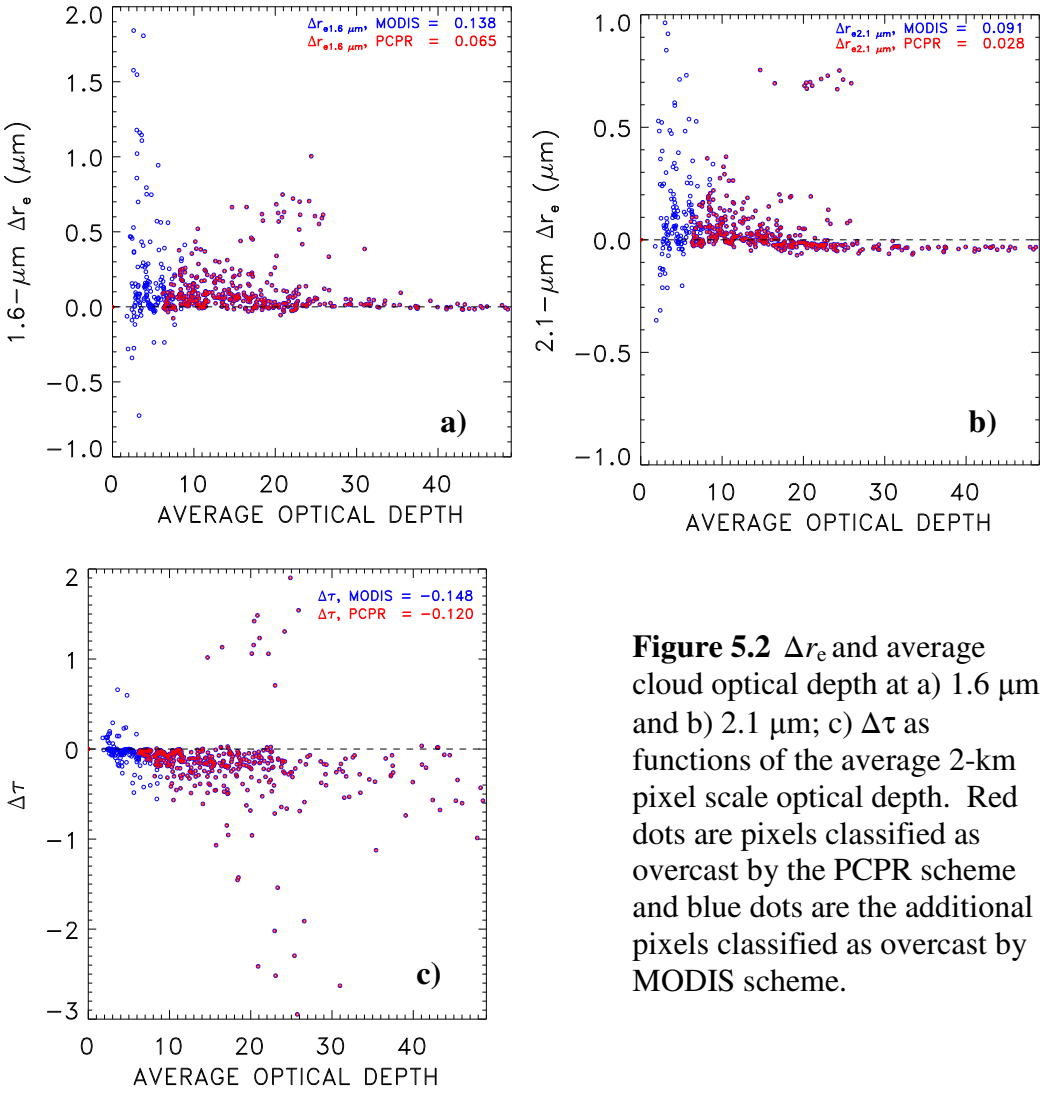

Figure 5.2 Δr_e and average cloud optical depth at a) 1.6 μm and b) 2.1 μm; c) $\Delta\tau$ as functions of the average 2-km pixel scale optical depth. Red dots are pixels classified as overcast by the PCPR scheme and blue dots are the additional pixels classified as overcast by MODIS scheme.

while for the partly cloudy pixel retrievals the droplet radii were 0.028 μm larger. Although both Δr_e were small, the PCPR scheme consistently produced smaller differences.

The MODIS overcast pixel identifications led to optical depths that were 0.148 smaller than the average for the 2-km pixels. The PCPR visible optical depth was 0.120 smaller than the average. For both MODIS and PCPR, $\Delta\tau$ is consistently an underestimate of the average optical depth.

5.1.2 Overcast Scene

The overcast region selected is shown in Figure 5.3. It was observed on 17 May, 2004 at 1141 UTC, located at 48.63º N, 11.54º W. The satellite zenith angle was 18.38º, the solar zenith angle was 31.84º, and the azimuth angle was 128.9º. The regional mean cloud cover for this scene was 1.0. Fig. 5.3 shows the same quantities as in Fig. 5.1, but for this nearly overcast scene.

In Fig. 5.3 the 2-km resolution appears coarser than the 500-m resolution. Nonetheless, the entire region was more consistently overcast, and so less of the variability in the 500-m data is lost when moving to 2-km resolution. The average regional cloud cover of 1.0 indicates that retrievals of cloud properties for this scene should not be greatly affected by broken clouds, and the number of pixels identified as overcast by the PCPR was not very different from the number classified as overcast by the MODIS cloud mask, as shown in Fig. 5.3 c). The red dots are PCPR overcast pixels and the blue dots are the additional pixels classified as overcast by the MODIS cloud mask. In contrast to Fig. 5.1 c), there are very few additional blue dots.

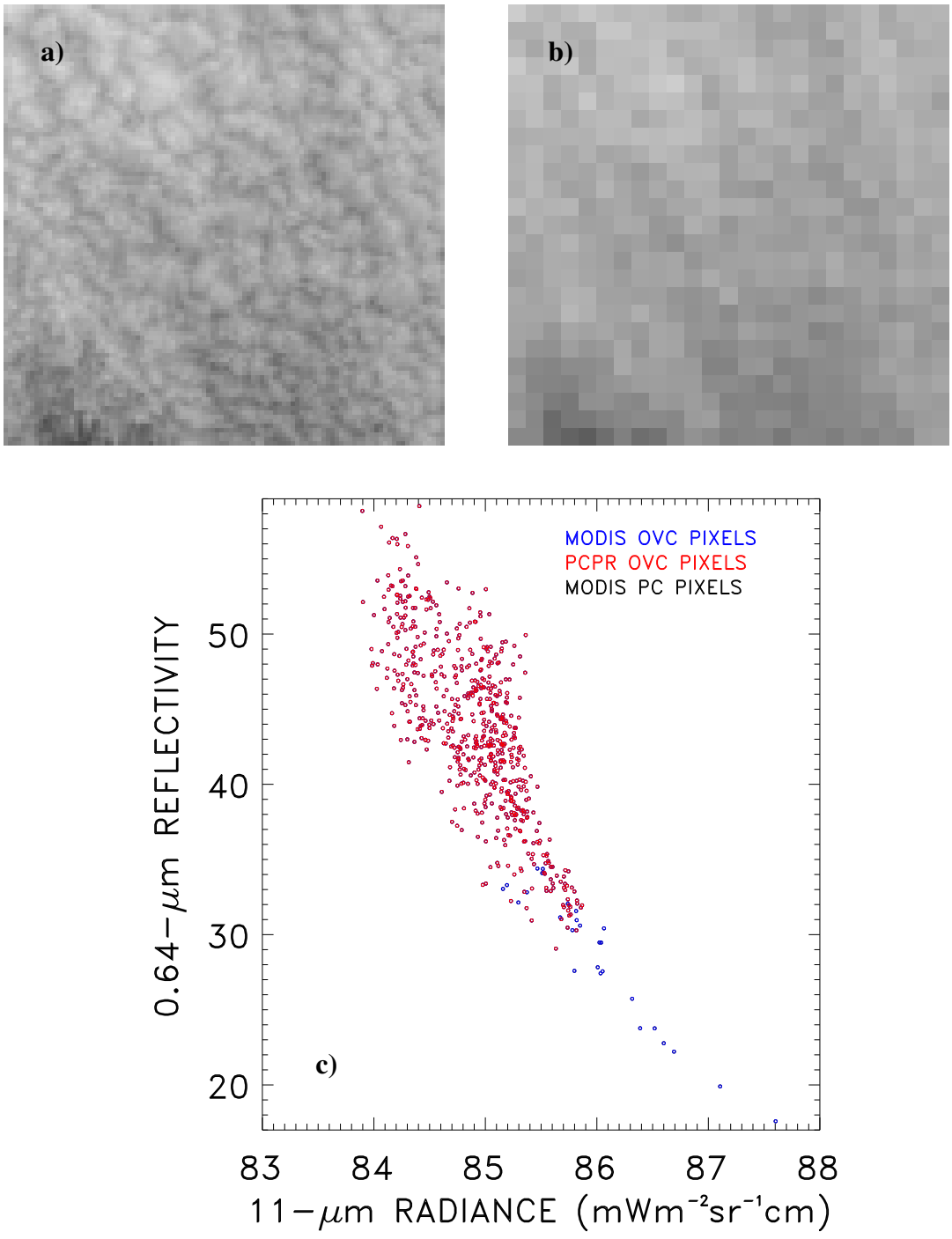

Figure 5.3 Same as for Figure 5.1, but for an overcast region.

Since the scene is nearly spatially uniform, the biases of 1.6-μm Δr_e, 2.1-μm Δr_e and $\Delta\tau$ were expected to be small. Additionally, since PCPR and MODIS do not differ significantly in their classification of overcast pixels in this region, the difference in biases for the two overcast pixel identification schemes was small. Fig. 5.4 shows a) 1.6-μm Δr_e, b) 2.1-μm Δr_e, and c) $\Delta\tau$ as functions of the 2-km pixel

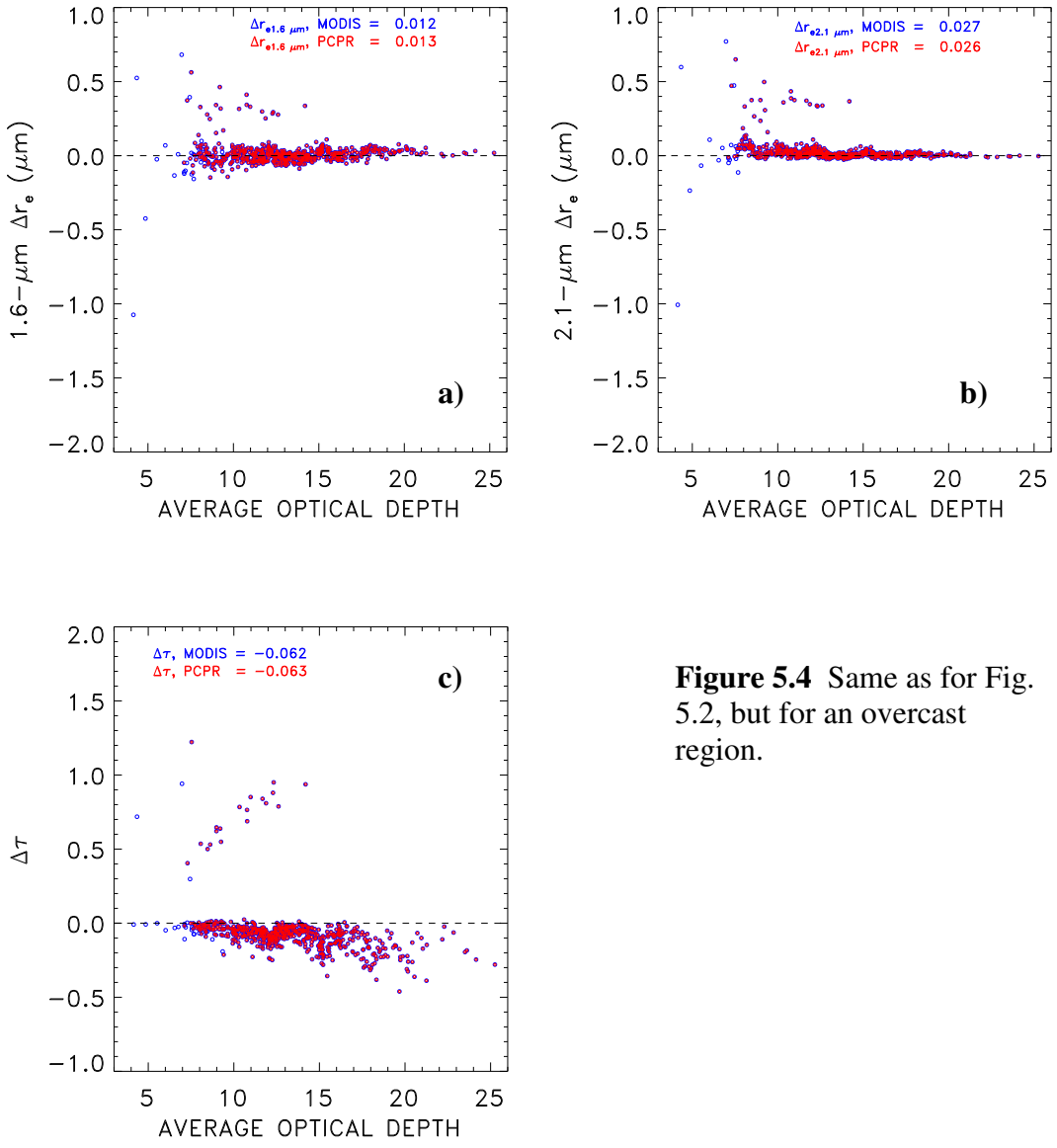

Figure 5.4 Same as for Fig. 5.2, but for an overcast region.

scale average optical depth. The variability in all three quantities was much smaller than that for the region with both overcast and partly cloudy pixels, and the biases were smaller as well.

The droplet radius was overestimated when using retrievals based on average reflectivities and the optical depth was underestimated, but the biases were small. Fig. 5.4 a), b) and c) also lack the outliers in the corresponding quantities that appear in Fig. 5.2, indicating that most pixels sampled from a highly overcast region had smaller biases and thus were more reflective of the actual cloud properties.

5.1.3 Partly Cloudy Scene

The partly cloudy region selected is shown in Figure 5.5. It was observed on 26 May, 2005 at 1145 UTC, located at 55.3º N, 11.43º W. The satellite zenith angle was 22.96º, the solar zenith angle was 35.72º, and the azimuth angle was 124.7º. The regional mean cloud cover for this scene was 0.56. Fig. 5.5 shows the same quantities as in Fig. 5.1, but for this partly cloudy scene.

The region contained many broken clouds, indicated by the dark areas in Fig. 5.5. Areas that contained relatively thick clouds were punctuated by holes in the cloud column. The 500-m resolution resolved some of these features, but the 2-km scale image lost much of the variation in visible reflectivities. Fig. 5.5 c) shows 11-μm radiance and 0.64-μm reflectivity for this region at the 2-km scale. The partly cloudy pixel retrievals identified few overcast pixels (red dots). These pixels were

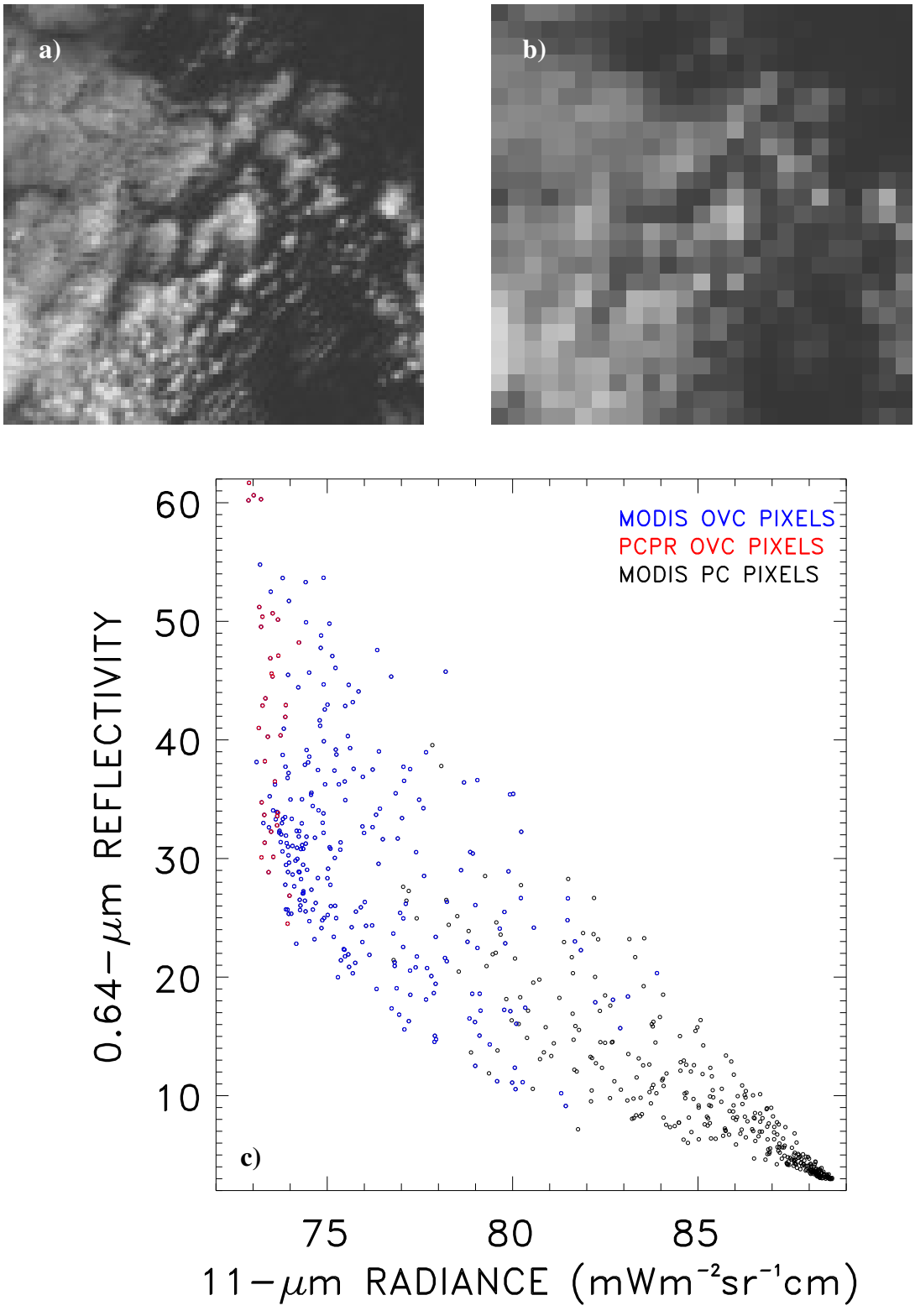

Figure 5.5 Same as for Fig. 5.1, but for a partly cloudy region.

located in the thickest clouds. The blue dots, representing pixels identified as overcast by the MODIS cloud mask, were much more numerous and extended to pixels with small 0.64-μm visible reflectivities. Many of these pixels were probably partially covered by clouds.

Owing to the relatively large spatial inhomogeneity, the biases in the retrieved optical depths and droplet radii were large and highly variable. Figure 5.6 shows Δr_e

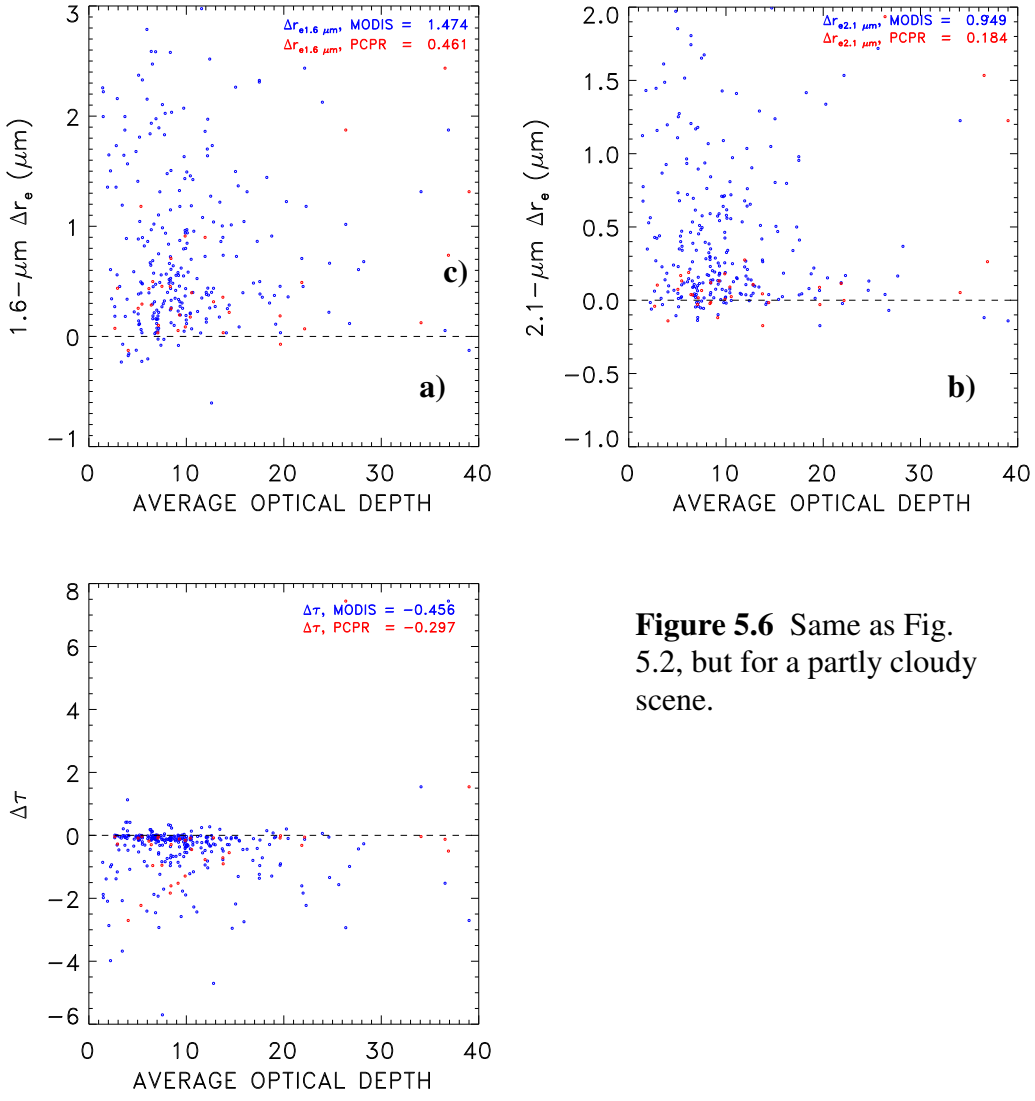

Figure 5.6 Same as Fig. 5.2, but for a partly cloudy scene.

for 1.6 and 2.1 μm and $\Delta\tau$ and the average optical depth for the 2-km scale. The biases were not only large but also much more variable between pixels than in either of the previous two cases. MODIS biases were substantially larger than the PCPR biases. The failures of the overcast pixel assumption imbedded in the MODIS cloud mask became more apparent. MODIS incorrectly classified many pixels as overcast, and the retrievals were thus heavily affected by the effects of spatial inhomogeneity. The horizontal variation in cloud cover and optical depth had an effect on the PCPR properties as well, but as the pixels selected as overcast by the PCPR were optically thick in the visible and exhibited less spatial inhomogeneity in the near infrared reflectances, the resulting biases were smaller.

5.2 Typical biases in retrievals of cloud properties

The case studies of section 5.1 were performed to illustrate the biases in the retrieved optical depths and droplet radii at the 2-km scale for different regions. Cloud properties are highly affected by the regional cloud cover, and whether the retrieval scheme accounts for the fractional coverage in the pixel (PCPR) or assumes all cloudy pixels are overcast when cloudy (MODIS). To judge the magnitudes of these effects at a larger scale, the quantities Δr_e and $\Delta\tau$ were accumulated from a survey of marine stratocumulus over the Northeastern Atlantic using the Terra MODIS observations. The analysis was divided into MODIS and PCPR identifications of overcast pixels for two types of regions: those overcast with regional mean cloud cover greater than 0.95,

and those containing broken clouds with cloud cover between 0.6 and 0.8. The cloud cover was obtained from the PCPR for the 1-km MODIS pixels. There were 1062 50-km scale regions with fractional cloud cover greater than 0.95, and 123 50-km scale regions with fractional cloud cover between 0.6 and 0.8.

5.2.1 Overcast Regions

For the regions found to be nearly overcast, with fractional cloud cover greater than 0.95, Figure 5.7 shows the total distributions at the 500-m scale of a) droplet radius retrieved using 1.6-μm reflectances, b) droplet radius retrieved using 2.1-μm reflectances, and c) optical depth as derived using the PCPR overcast pixel identification (red solid line) and MODIS identification (blue dotted line). According to the trend suggested by the results from the case studies, the biases in MODIS retrievals were expected to be greater than those for the PCPR. As expected the droplet radii retrieved using the MODIS overcast pixel identifications were larger than those obtained using the PCPR scheme, and the optical depths were smaller. Since this data was taken from nearly overcast regions, the differences obtained using the MODIS and PCPR overcast pixel identifications were expected to be relatively small, and the biases for both methods were expected to be less severe than those obtained for the partly cloudy scenes.

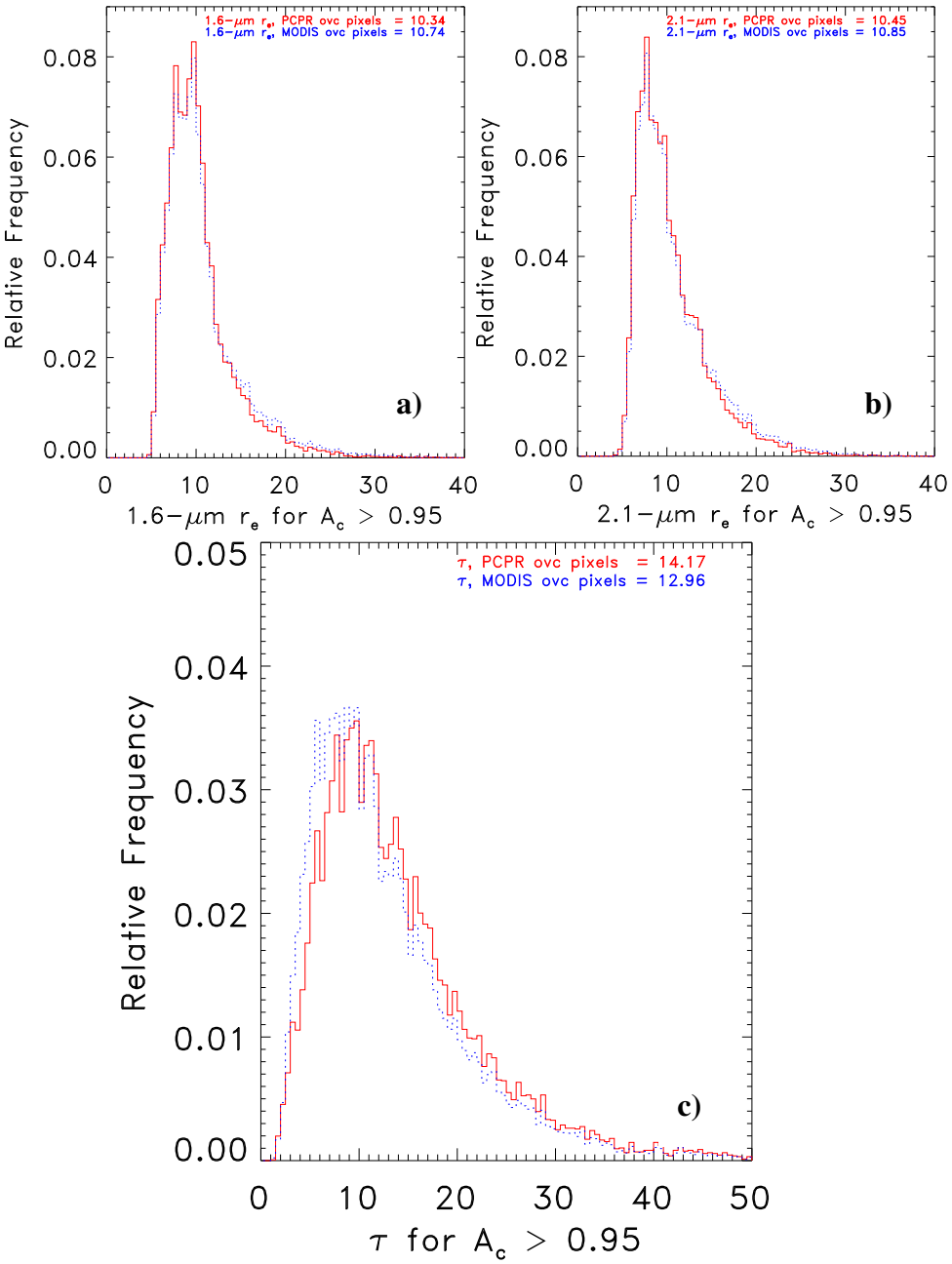

Figure 5.7 Total distributions of a)1.6-μm droplet radius, b) 2.1-μm droplet radius, and c) optical depth as derived by PCPR (red solid line) and MODIS (blue dotted line) identifications of overcast pixels in regions with $A_c > 0.95$. The regional cloud cover was derived using the PCPR scheme applied to 1-km MODIS pixels.

Figure 5.8 shows Δr_e for 1.6 μm obtained with the MODIS overcast pixel identification, a), with the PCPR identification, b), Δr_e for 2.1 μm obtained with the MODIS identifications c), with the PCPR identification, d), $\Delta\tau$ for MODIS, e), and for PCPR, f). In each frame, the red represents the quantity for the upper third of optical depths (the thickest one third of clouds) and blue represents the quantity for the lower third of optical depths (the thinnest one third of clouds).

In overcast regions, MODIS and PCPR retrievals do not differ significantly, and the biases obtained using both overcast pixel identification schemes were small. The results obtained for the optically thickest third of the clouds using both the MODIS and PCPR overcast pixel identifications were similar. For the thinnest third of the clouds in the overcast regions, the biases for droplet radii and optical depths increased, yet the results obtained with the MODIS and PCPR overcast pixel identifications were consistent with each other. For the thinnest third of clouds, the bias in optical depth retrievals, however, actually became positive. Optical depth was consistently underestimated for both the MODIS and PCPR identifications of overcast pixels, yet for the thinnest clouds the optical depths were actually overestimated slightly. According to Marshak et al. (2005), this may be due to 3D radiative effects within cloud pixels. Even at very small spatial scales, Marshak et al. (2005) have shown that a non-vanishing horizontal flux is present between pixels.

Figure 5.9 shows $d\ ln\ r_e / d\ ln\ \tau$ for the regions overcast by marine stratocumulus. There are two anticipated effects at work. The first is that the MODIS identification of overcast pixels is less stringent than that used in the PCPR scheme.

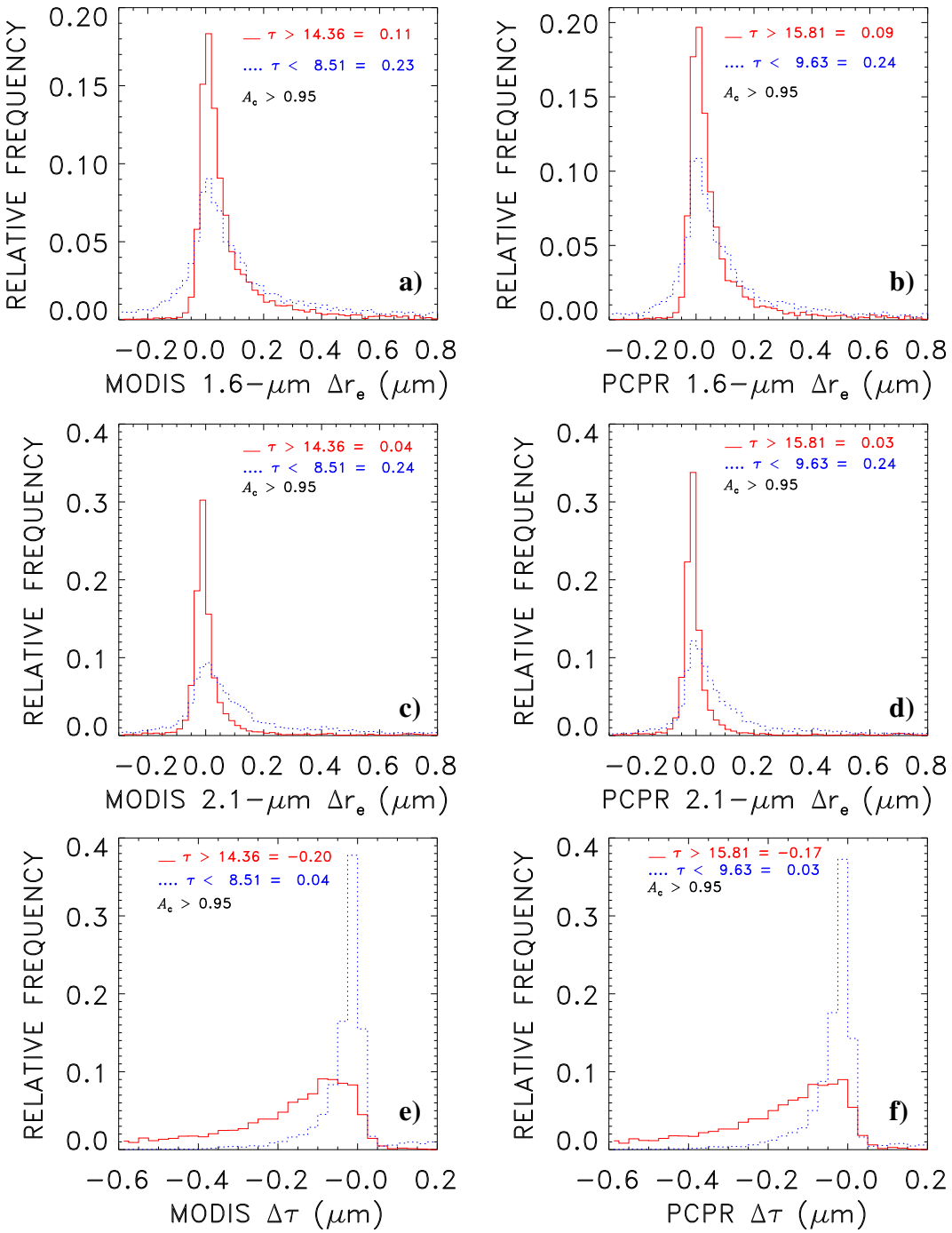

Figure 5.8 Δr_e for 1.6 μm obtained with the MODIS overcast pixel identification, a), with the PCPR identification, b), Δr_e for 2.1 μm obtained with the MODIS identification, c), with the PCPR identification, d), $\Delta\tau$ for MODIS, e), and for PCPR, f). The red solid lines represent the quantity for the upper third of the optical depths (the thickest one third of clouds) and blue dotted lines represent the quantity for the lower third of optical depths (the thinnest one third of clouds) for the 2-km pixels.

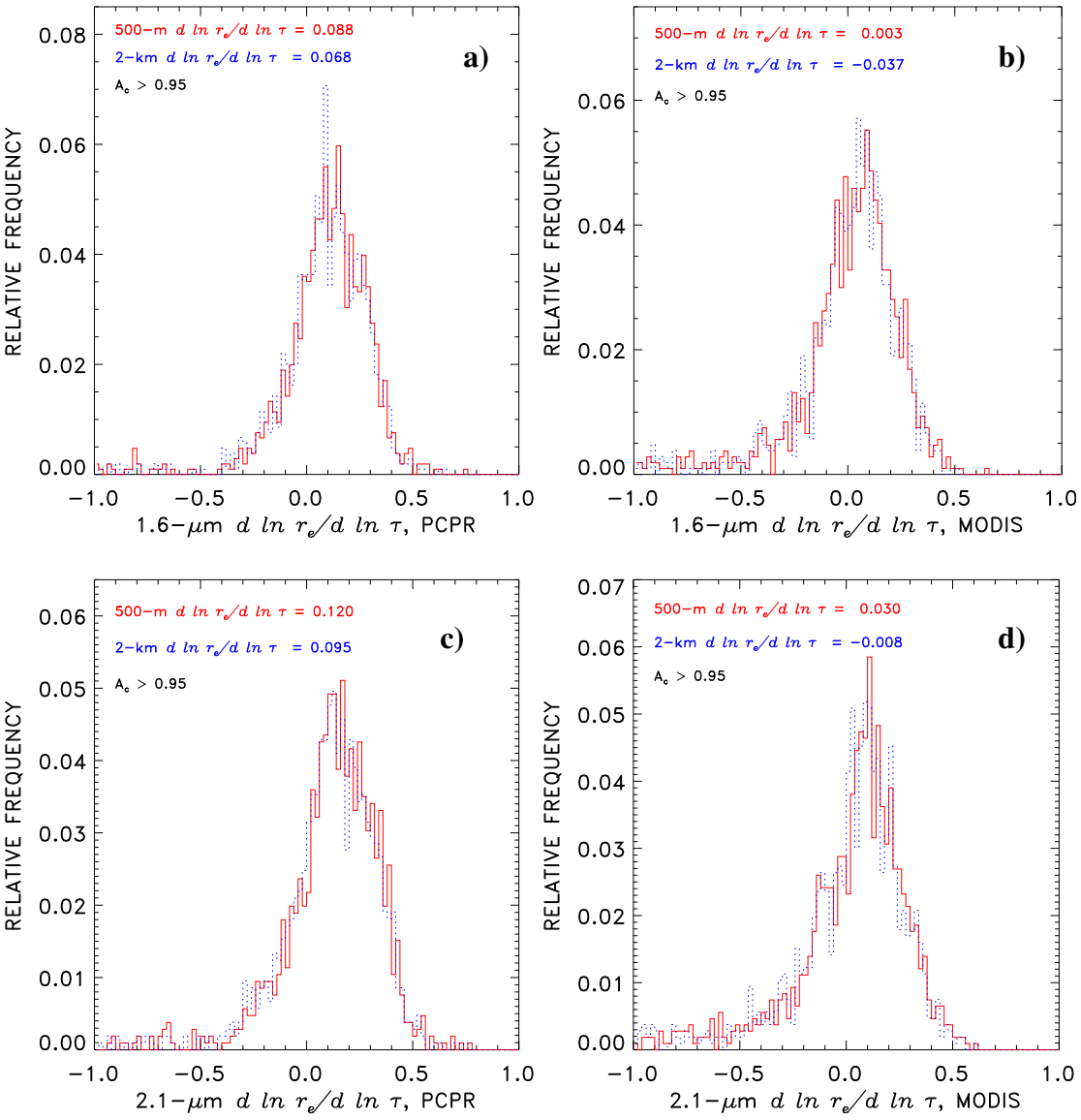

Figure 5.9 $d \ln r_e / d \ln \tau$ using 1.6-μm reflectance and the PCPR identifications of overcast pixels, a), MODIS identifications, b), 2.1-μm reflectances and the PCPR identifications, c), and the MODIS identifications, d). All values are for regions with fractional cloud cover greater than 0.95.

The MODIS scheme can identify pixels with only partial cloud cover as overcast. The $d \ln r_e / d \ln \tau$ values obtained using the PCPR identifications were noticeably closer to that expected for adiabatic clouds than those obtained using the MODIS

identifications. Additionally, the $d \ln r_e / d \ln \tau$ values obtained using the 500-m data were closer to the adiabatic value of 0.2 than those obtained using the 2-km average radiances. The effects of horizontal inhomogeneity were less pronounced in the 500-m reflectivities.

5.2.2 Regions of Broken Clouds

For regions with fractional cloud cover between 0.6 and 0.8, Fig. 5.10 shows the distributions of droplet radius retrieved using 1.6-μm reflectances, a), droplet radius retrieved using 2.1-μm reflectances, b), and visible optical depth, c). As expected from the results of the case studies, the droplet radii obtained for the pixels identified as overcast by MODIS were larger than those for the pixels identified as overcast by the PCPR scheme. Optical depths obtained for the pixels identified as overcast by MODIS were also less than the optical depths obtained for pixels classified as overcast by the PCPR scheme. Likewise, the differences in the retrieved properties were greater than those obtained for the overcast regions. These increases occurred because the biases increased with the greater spatial variability.

Figure 5.11 shows Δr_e for 1.6 μm using the MODIS overcast pixel identifications, a), using the PCPR identifications, b), Δr_e for 2.1 μm using the MODIS identifications, c), using the PCPR identifications, d), $\Delta \tau$ using the MODIS identifications, e), and using the PCPR identifications, f). The red solid lines represent

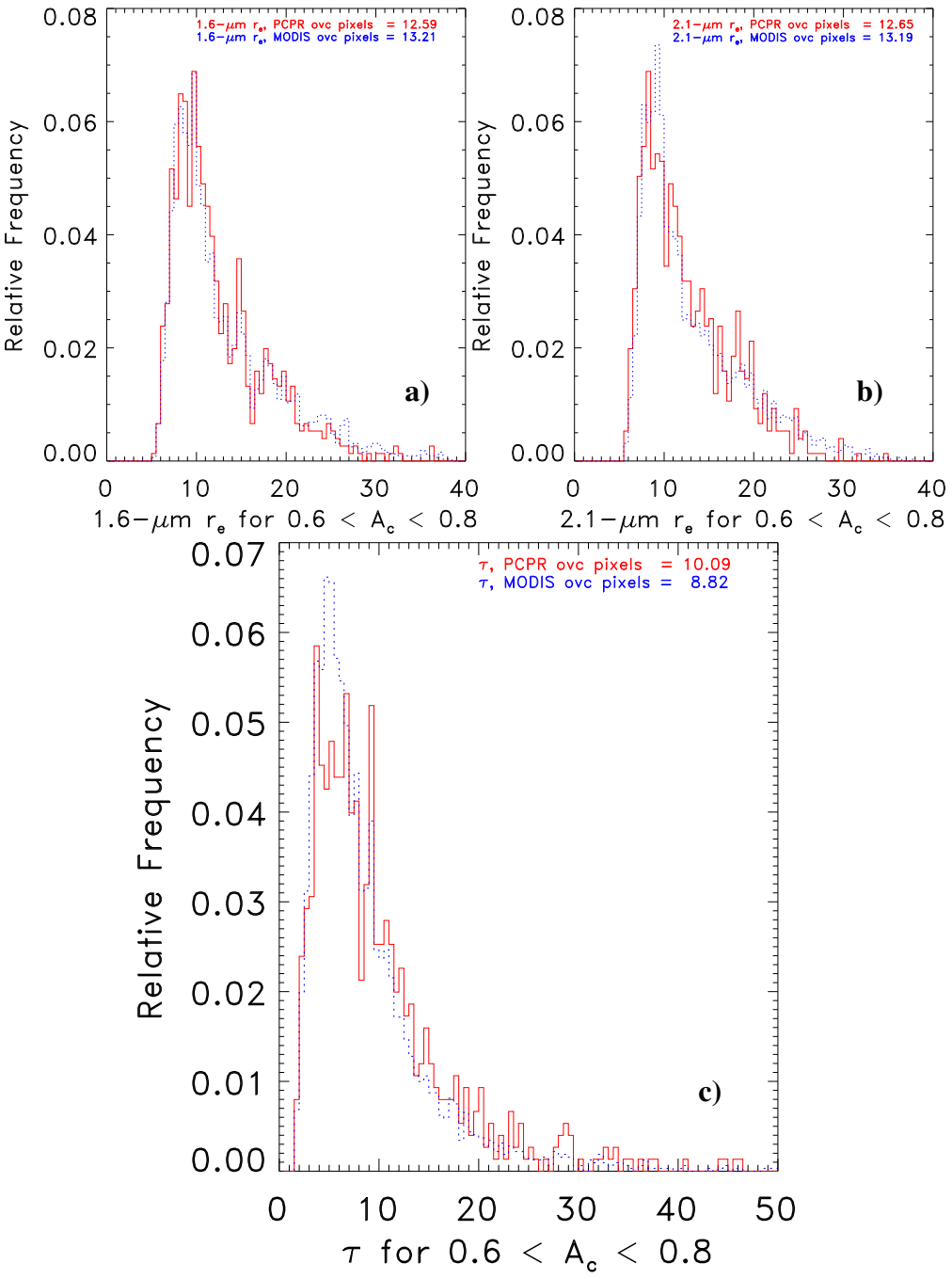

Figure 5.10 Same as Fig. 5.7, but for regions containing broken clouds with fractional cloud cover between 0.6 and 0.8 as obtained with the PCPR scheme.

the quantity for the upper third of optical depths (the thickest one third of clouds) and blue dotted lines represent the quantity for the lower third of optical depths (the

thinnest one third of clouds). Biases obtained using both the MODIS and the PCPR identifications of overcast pixels increased for the regions containing broken clouds.

In the broken cloud regions, PCPR identifications of overcast pixels led to more accurate droplet radii and optical depths than the MODIS identifications for the thickest third of the clouds. On the other hand, for the thinnest third of the clouds, the PCPR overcast pixel identifications led to larger biases in droplet radii than were obtained for the MODIS identifications. One possible explanation for these differences could be that the reflectivities at both the visible and the near infrared wavelengths became more linear with optical depth as the optical depth became smaller, thereby reducing the nonlinearities that gave rise to the biases.

Figure 5.12 shows the values of $d \ln r_e / d \ln \tau$ calculated for the MODIS and PCPR identifications using 1.6 and 2.1-μm reflectivities for the regions with broken clouds. While the average $d \ln r_e / d \ln \tau$ for the overcast regions were generally positive, for the regions with broken clouds, positive values were obtained only when using the PCPR overcast pixel identifications. When using MODIS identifications, the $d \ln r_e / d \ln \tau$ were negative. Consistent with the $d \ln r_e / d \ln \tau$ in overcast regions, the 500-m resolution gave values closer to those expected of adiabatic clouds than were obtained for the 2-km resolution.

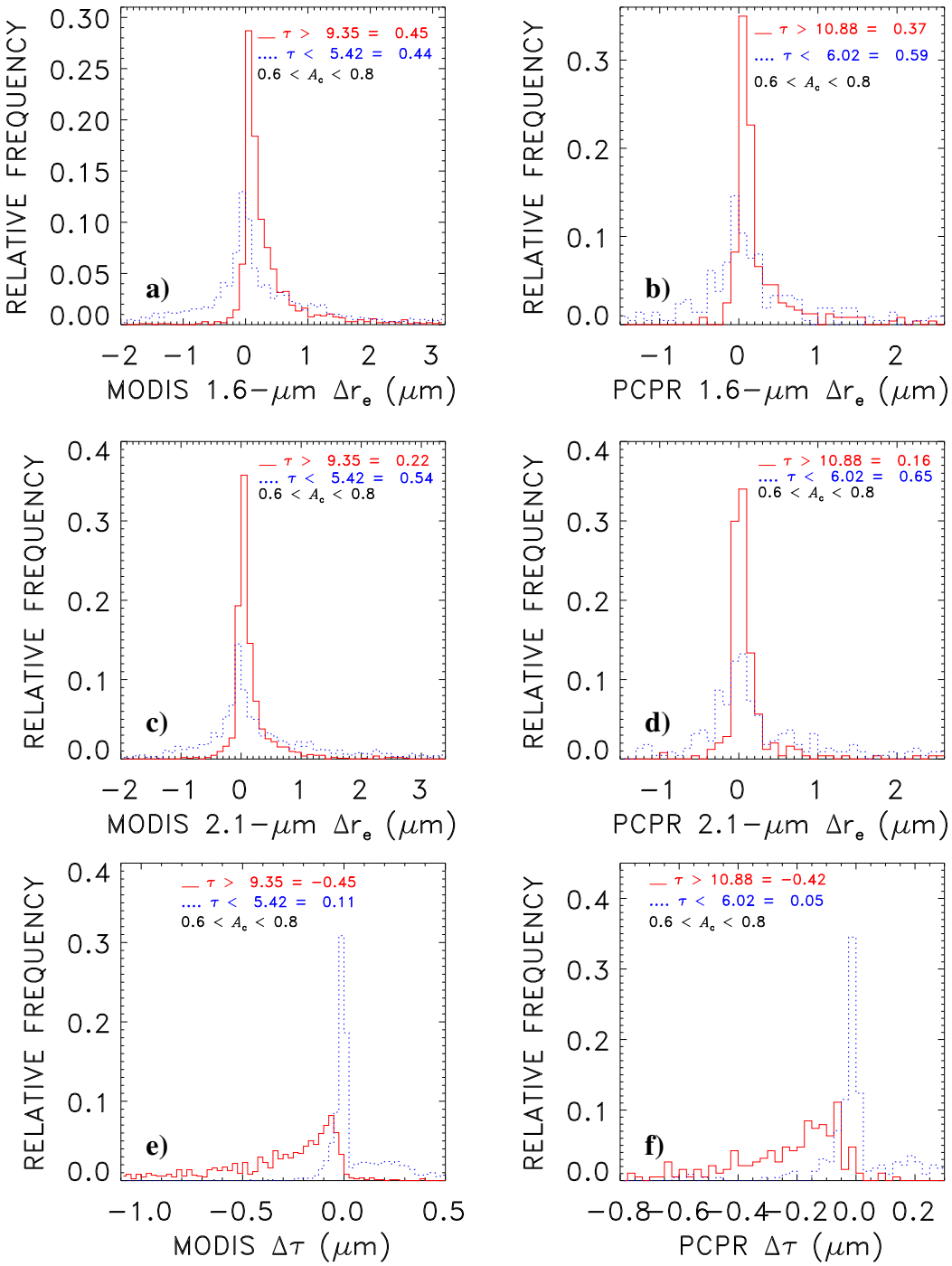

Figure 5.11 Same as Fig. 5.8, but for the regions of broken clouds with $0.6 < A_c < 0.8$ as obtained with the PCPR scheme.

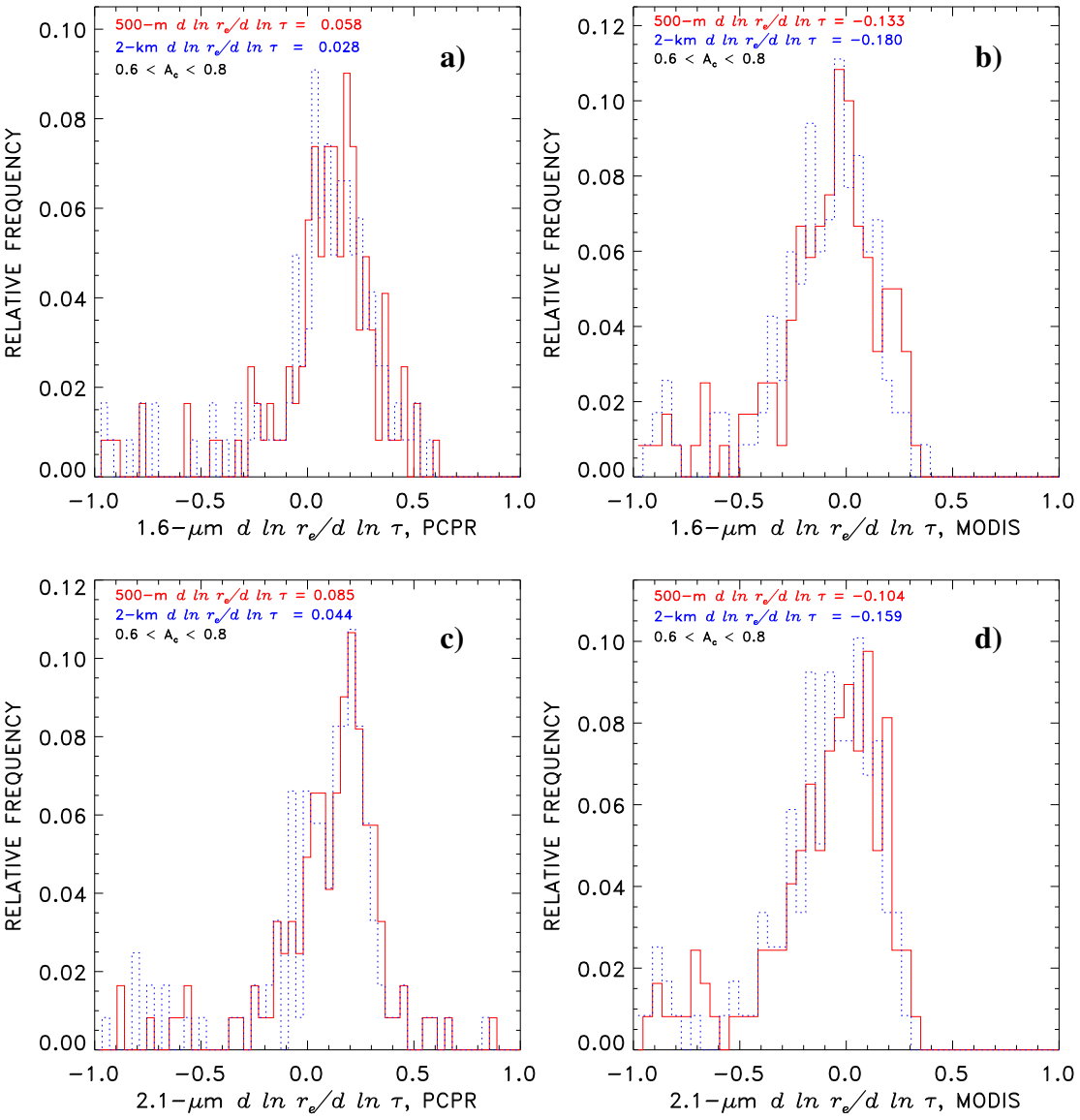

Figure 5.12 Same as Figure 5.9, but for the regions with broken clouds.

In order to assess the statistical significance of the bias between overcast regions and regions containing broken clouds for MODIS and PCPR identifications, the $\Delta\tau$, $\Delta r_{e2.1}$, and $\Delta r_{e1.6}$ were calculated using regional means. In each region, both the properties for the pixels with optical depths falling in the thinnest third of clouds and the properties for the pixels with optical depths falling within the thickest third of

clouds were averaged to obtain regional mean values for $\Delta\tau$, $\Delta r_{e2.1}$ and $\Delta r_{e1.6}$. The pixel-scale distributions in Fig. 5.8 and 5.11 provided information on pixel-scale biases, but pixels cannot be considered as being statistically independent. Cloud properties exhibit correlations among neighboring pixels. The mean properties for 50-km scale regions were, on the other hand, assumed to be statistically independent. Computing the regional mean biases for the pixels contributing to the thickest third of clouds and thinnest third of clouds allowed for an assessment of the statistical significance of the differences. In Table 5.1, the biases for MODIS and PCPR identifications of overcast pixels for overcast regions and regions containing broken clouds are shown for the thinnest and thickest third of clouds. For each parameter $\Delta\tau$, $\Delta r_{e2.1}$ and $\Delta r_{e1.6}$, the mean and standard error are given, as well as 90% confidence levels for the mean. The standard error is calculated by dividing the standard deviation of a sample by the square root of the sample size. The 90% confidence level is an interval estimate of the mean bias and is simply calculated by adding and subtracting from the mean the standard error multiplied by a factor determined from a t-distribution table (Ramsey and Schafer, 2002). Also shown are the numbers of regions contributing to the means. When regional mean biases were computed using only the pixels that contributed to the thinnest third and thickest third of clouds, the biases were larger than those computed at the pixel-scale. Additionally, the differences between the biases for MODIS and PCPR identification of overcast pixels were greater than at the pixel-scale, and the biases for both MODIS and PCPR identifications for regions containing broken clouds were dramatically larger than

those for overcast regions. At the 90% confidence level, all biases were statistically significant and not equal to zero

Parameter	Overcast Regions		Broken-Cloud Regions	
	Partly Cloudy Pixel Retrievals (PCPR)			
Optical Depths	$\tau > 15.81$	$\tau < 9.63$	$\tau > 10.88$	$\tau < 6.02$
Number of Regions	809	811	67	37
$\Delta r_{e1.6}$ (μm)	0.156 ± 0.008 [0.143, 0.169]	0.197 ± 0.0097 [0.181, 0.213]	0.420 ± 0.052 [0.335, 0.51]	0.528 ± 0.12 [0.33, 0.726]
$\Delta r_{e2.1}$ (μm)	0.0512 ± 0.0061 [0.0411, 0.0613]	0.179 ± 0.0092 [0.164, 0.195]	0.181 ± 0.032 [0.128, 0.234]	0.571 ± 0.12 [0.373, 0.777]
$\Delta\tau$	-0.0857 ± 0.015 [-0.11, -0.061]	0.0353 ± 0.0052 [0.027, 0.044]	-0.262 ± 0.043 [-0.333, -0.191]	0.0514 ± 0.027 [0.0069, 0.096]
	MODIS			
Optical Depths	$\tau > 14.36$	$\tau < 8.51$	$\tau > 9.35$	$\tau < 5.42$
Number of Regions	814	821	100	103
$\Delta r_{e1.6}$ (μm)	0.181 ± 0.0082 [0.167, 0.195]	0.351 ± 0.023 [0.313, 0.289]	0.531 ± 0.066 [0.422, 0.64]	1.13 ± 0.15 [0.882, 1.38]
$\Delta r_{e2.1}$ (μm)	0.0667 ± 0.0055 [0.0576, 0.0757]	0.326 ± 0.019 [0.295, 0.357]	0.277 ± 0.043 [0.206, 0.348]	1.06 ± 0.12 [0.862, 1.26]
$\Delta\tau$	-0.125 ± 0.016 [-0.151, -0.099]	0.103 ± 0.0089 [0.0883, 0.118]	-0.269 ± 0.047 [-0.347, -0.191]	0.0246 ± 0.02 [-0.0084, 0.0576]

Table 5.1 Biases for MODIS and PCPR identifications of overcast pixels in regions overcast by marine stratocumulus and regions containing broken clouds. Means ± standard errors of the means along with 90% confidence levels in brackets are given.

with the largest biases occurring for the thinnest third of clouds in regions containing broken clouds, especially when the MODIS cloud flag was used to identify overcast pixels. Also consistent with the results from the pixel-scale distribution is the overestimate of droplet radius and underestimate of optical depth. Optical depth from

regions containing broken clouds was on average approximately 4 smaller than optical depths from overcast regions, while droplet radii were approximately 2 μm larger.

CHAPTER 6
CONCLUSIONS

A radiative transfer and cloud property retrieval scheme was developed for assessing the impacts of vertical and spatial variations of cloud properties within imager pixels on the retrievals of cloud optical depth and droplet radius. The radiative transfer scheme used the Eddington Approximation for multiple scattering and results were presented for single-layered scenes overcast by marine stratocumulus in which the vertical profile of droplet radius was modeled by the adiabatic ascent of moist air. For relatively thick adiabatic clouds, droplets grow as $H^{1/3}$, where H is height above the lifting condensation level. Reflectances for vertically uniform clouds were used to retrieve the cloud optical depth and droplet radius for adiabatic clouds. Optical depth is a non-dimensional parameter that measures the extinction of light within a medium. The retrievals were based on the 0.64, 1.6, 2.1, and 3.7-μm channels available with MODIS imagery. The droplet radii retrieved using 3.7-μm reflectances were close to the cloud top droplet radius calculated assuming adiabatic ascent. Absorption at 3.7 μm is relatively large, and photons cannot travel as deeply into the cloud without being absorbed. Penetration depths for photons at 2.1 μm are slightly larger than those for photons at 3.7 μm. Penetration depths are even larger for photons at 1.6 μm. Droplet radius retrieved using the simulated 1.6-μm reflectance was the smallest, and deviated the most from the cloud top droplet radius. For spatially uniform clouds, the range of droplet radii retrieved for the three near infrared wavelengths was

approximately 1 μm for visible optical depths less than approximately 40. The simulated retrievals indicated at all cloud thicknesses that the r_e derived using the 3.7-μm reflectances should be the largest, followed by the r_e derived using the 2.1-μm reflectances and 1.6-μm reflectances. These results were inconsistent with retrievals based on MODIS reflectances for pixels identified as being overcast by marine stratus. The MODIS observations produced the largest droplets when using the 2.1 μm reflectances.

The retrieval based on reflectances for vertically uniform clouds, on the other hand, produced optical depths that were identical to those for adiabatic clouds. The retrieval scheme formulated in this thesis used visible reflectances to obtain optical depths once the droplet radius was determined. Visible reflectances are a function of optical depth and asymmetry parameter, g. Since g is only a weak function of droplet radius, the visible reflectance calculated for an adiabatic cloud with growing droplet radius differs little from that obtained for a vertically uniform cloud.

Values of $d \ln r_e / d \ln \tau$ retrieved using the simulated 1.6, 2.1, and 3.7-μm reflectances were not consistent with MODIS observations. For spatially uniform clouds adiabatic cloud development led to $d \ln r_e / d \ln \tau$ retrieved at all near infrared wavelengths that were greater than 0.2, especially for optically thin clouds. The $d\ ln\ r_{e,1.6\text{-}\mu m}/d\ ln\ \tau$ was largest, followed by $d\ ln\ r_{e,2.1\text{-}\mu m}/d\ ln\ \tau$ and then the $d\ ln\ r_{e,3.7\text{-}\mu m}/d\ ln\ \tau$. For large optical depths, the $d \ln r_e / d \ln \tau$ calculated using the simulated1.6, 2.1, and 3.7-μm reflectances converged to approximately 0.2. Observations from Aqua MODIS confirmed that scenes overcast by optically thick

marine stratocumulus conform to an adiabatic $d \ln r_e / d \ln \tau$ of 0.2, but regions containing broken clouds yielded 1.6-μm and 2.1-μm derived $d \ln r_e / d \ln \tau$ that were far less than 0.2 (Hayes et al. 2009). The results of this simulation suggested that either broken marine stratocumulus were not adiabatic, or that errors in the retrieved cloud properties hid the true values of $d \ln r_e / d \ln \tau$.

The radiative transfer scheme accounting for vertically non-uniform clouds was modified to account for horizontal inhomogeneity within each imager pixel. The method was formulated using the Independent Pixel Approximation described by Cahalan (1994). Realistic distributions of optical depth with means given by MODIS pixel-scale optical depths and a variance based on LES models of marine stratocumulus given by Kato et al. (2006) were used to represent the subpixel variations in optical depth in a cloud. The simulation used a uniform distribution of droplet radius at the cloud base and constant number concentration taken from observations by Brenguier et al. (2003). Each subpixel was allowed to grow following the adiabatic ascent of moist air until it reached the appropriate optical depth. The average values retrieved for the subpixels were compared to retrieved properties based on average reflectances. The retrievals using 1.6-μm reflectances were most strongly affected by the addition of subpixel variation in optical depth. Mean droplet radius retrieved in the simulation using 1.6-μm reflectances was the largest, followed by the droplet radius derived from 2.1-μm and 3.7-μm reflectances. The simulation of large droplet radii at the smaller-wavelengths indicated that the large droplets observed in MODIS may have resulted from the assumption that clouds are horizontally uniform.

Due to the nonlinear relationship between reflectances and cloud properties, this assumption and the subpixel variability led to biases in the retrievals. For a pixel that contains a cloud with a distribution of optical depths, the retrieved optical depth is smaller than the average optical depth, and retrieved droplet radius is larger than the average droplet radius.

The values of $d \ln r_e d \ln \tau$ calculated by taking into account horizontal non-uniformity were consistent with adiabatic ascent. They produced mean values close to 0.2 for droplet radii retrieved using the three near infrared wavelengths. While the simulation taking into account the vertical distributions of droplet radius produced $d \ln r_e d \ln \tau$ that were greater than 0.2, the addition of subpixel variability in the optical depths and droplet radii produced values that were both greater than and less than 0.2, as did the retrievals based on MODIS reflectances.

The vertically and horizontally inhomogeneous cloud property retrieval scheme detailed in this thesis came close to explaining the droplet radii and optical depths retrieved from MODIS. Growth of cloud droplets by adiabatic ascent given realistic distributions of optical depth were accounted for, but there is room for improvement and future work. Cloud droplet formation depends on the number of available cloud condensation nuclei, the available water vapor, and the updraft velocities, all of which vary spatially within a 1-km pixel. The retrieval scheme developed in this thesis used constant cloud base droplet radius and number concentration. A distribution of cloud base droplet radii or droplet number

concentrations could easily be added and might yield distributions of r_e and $d \ln r_e / d \ln \tau$ closer to those observed.

Visible optical depth and droplet radius retrieved using the 0.64, 1.6, and 2.1-μm reflectivities were obtained from MODIS 500-m data. The 500-m pixels were aggregated into 2-km scale pixels in order to study the role of spatial variation in cloud property retrievals. The biases, calculated by taking the difference of properties retrieved based on average reflectances and the average of the subpixel properties were calculated for varying amounts of cloud cover using both the MODIS cloud processing and PCPR schemes to identify overcast pixels. For typical scenes that contained a mix of partly cloudy and overcast pixels, the PCPR classification incurred smaller biases when retrieving optical depth and droplet radius than the MODIS classification because the PCPR was more stringent in its identification of overcast pixels and only classified the most optically thick pixels as overcast. The optically thick pixels exhibited less subpixel spatial variability than the thinner broken clouds. MODIS classified pixels as overcast if clouds were detected in the field of view. Consequently, the MODIS scheme often identified pixels that were either optically thin or partly cloudy.

For 50-km scale regions nearly overcast by marine stratus, the biases for both the MODIS and PCPR overcast pixel identifications were small. The impacts of spatial variation in cloud properties was more prominent in clouds that were optically thinner. The values of $d \ln r_e / d \ln \tau$ obtained using both the MODIS and PCPR identifications showed two effects. The MODIS identifications produced

$d \ln r_e / d \ln \tau$ that were further from the value of 0.2 expected for adiabatic clouds than the PCPR identifications. Consistent with the bias incurred by performing retrievals based on average radiances, the $d \ln r_e / d \ln \tau$ obtained using the 500-m data were closer to the adiabatic value of 0.2 than those obtained for the 2-km pixels.

For the 50-km scale regions that were partially covered by a single layer of marine stratocumulus, the biases became larger. Both the MODIS and PCPR overcast pixel identifications led to large biases in the retrieved droplet radii and optical depths. When a region contained broken clouds, many pixels were likely to be partly covered by cloud. MODIS classified many of these pixels as overcast, and so the MODIS identifications were subjected to the influences of optically thin and broken clouds more so than the PCPR identifications, which selected pixels with optically thicker clouds as being overcast. Consequently, the MODIS overcast pixel identifications led to larger biases than obtained with the PCPR identifications. The values of $d \ln r_e / d \ln \tau$ obtained for the regions containing broken clouds were far from the value of 0.2 expected for the adiabatic ascent of moist air. While the average $d \ln r_e / d \ln \tau$ for overcast regions was generally positive, in the regions with broken clouds, only the PCPR identifications produced positive $d \ln r_e / d \ln \tau$. MODIS identification of overcast pixels led to a negative $d \ln r_e / d \ln \tau$. Consistent with the results from the overcast regions, the values of $d \ln r_e / d \ln \tau$ obtained from the 500-m overcast pixels were in closer conformity with the value expected for adiabatic clouds

than those obtained using the 2-km pixels for both the MODIS and PCPR identifications.

When mean regional biases based on pixels within the thinnest third of clouds and pixels within the thickest third of clouds were calculated, the effect of spatial variability was more pronounced. Biases calculated at all wavelengths for both MODIS and PCPR identifications of overcast pixels were larger and statistically different from zero at the 90% confidence level. In overcast regions, the PCPR method of identifying overcast pixels incurred smaller biases in droplet radii and optical depths than the MODIS cloud flag identifications, especially within the thinnest third of clouds. In regions containing broken clouds, biases for both MODIS and PCPR methods of identifying overcast pixels increased dramatically, but the PCPR scheme consistently retrieved cloud properties with smaller biases. The largest biases occurred when using MODIS to identify overcast pixels in the thinnest third of clouds within regions containing broken clouds.

BIBLIOGRAPHY

Baker, M.B., R.G. Corbin, and J Latham, 1980: The influence of entrainment on the evolution of cloud droplet spectra: I. A model of inhomogeneous mixing. *Quarterly Journal of the Royal Meteorology Society*, **106**, 581-597.

Barker, H.W., 1996: A Parameterization for Computing Grid-Averaged Solar Fluxes for Inhomogeneous Marine Boundary Layer Clouds. Part I: Methodology and Homogeneous Biases. *Journal of Atmospheric Sciences*, **53**, 2289-2303.

Bennartz, R., 2007: Global Assessment of marine boundary layer cloud droplet number concentration from satellite. *Journal of Geophysical Research*, **112**, doi:10.1029/2006JD007547, D02201.

Boers, R., J.R. Acarreta, and J.L. Gras, 2006: Satellite Monitoring of the first indirect aerosol effect: Retrieval of the droplet number concentration of water clouds. *Journal of Geophysical Research*, **111**, doi:10.1029/2006JD006838, D22208.

Brenguier, J., H. Pawlowska and L. Schüller, 2003: Cloud microphysical and radiative properties for parameterization and satellite monitoring of the indirect effect of aerosol on climate. *Journal of Geophysical Research*, **108**(D15), doi:10.1029/2002JD002682, 8632.

Burnet, F. and J.L. Brenguier, 2006: Observational Study of the Entrainment-Mixing Process in Warm Convective Clouds. *Journal of Atmospheric Sciences*, **64**, 1995-2011.

Cahalan, R.F, 1994: The Albedo of Fractal Stratocumulus Clouds. *Journal of Atmospheric Sciences,* **51**, 2434-2456.

Chang, F and Z. Li, 2002: Estimating the vertical variation of cloud droplet effective radius using multispectral near-infrared satellite measurements. *Journal of Geophysical Research*, **107**, doi:10.1029/2001JD000766, D000766.

Chang, F and Z. Li, 2003: Retrieving vertical profiles of water-cloud droplet effective radius: Algorithm modification and preliminary application. *Journal of Geophysical Research*, **108**, doi:10.1029/2003JD003906, D003906.

Coakley, J.A. Jr., M.A. Friedman, and W.R. Tahnk, 2004: Retrieval of Cloud Properties for Partly Cloudy Imager Pixels. *Journal of Atmospheric and Oceanic Technology*, **22**, 3-17.

Eitzen, Z.A., K.M. Xu, and T. Wong, 2007: Statistical Analyses of Satellite Cloud Object Data from CERES. Part V: Relationships Between Physical Properties of Boundary–layer Clouds. *Journal of Climate*, **21**, 668.

Hartmann, D.L, 1992: The Effect of Cloud Type on Earth's Energy Balance: Global Analysis. *Journal of Climate*, **5**, 1281.

Hartmann, D.L. *Global Physical Climatology*. San Diego: Academic Press, 1994.

Hayes, C.R., J.A. Coakley, Jr., and W.R. Tahnk, 2009: Properties of Marine Stratocumulus Derived from Collocated CALIPSO and MODIS Observations. Submitted to *Journal of Geophysical Research* issue on CALIPSO.

Kato, S., L. Hinkelman, and A. Cheng, 2006: Estimate of satellite-derived cloud optical thickness and effective radius errors and their effect on computed domain-averaged irradiances. *Journal of Geophysical Research*, **111**, doi:10.1029/2005JD006668, D006668.

Marshak, A., S. Platnick, G. Wen, and R.F. Cahalan, 2006: Impact of three-dimensional radiative effects on satellite retrievals of cloud droplet sizes. *Journal of Geophysical Research*, **111**, doi:10.1029/2005JD006686, D006686.

Marshak, A., L. Oreopoulos, A.B. Davis, W.J. Wiscombe, and R.F. Cahalan, 1999: Horizontal radiative fluxes in clouds and the accuracy of the Independent Pixel Approximation at absorbing wavelengths. *Geophysical Research Letters*, **26**, 1585-1588.

Matheson, M.A., J.A. Coakley, Jr., and W.R. Tahnk, 2005: Aerosol and cloud property relationships for summertime stratiform clouds in the northeastern Atlantic from Advanced Very High Resolution Radiometer observations. *Journal of Geophysical Research*, **110**, D24204, doi:10.1029/2005JD006165.

Miles, N.L, J. Verlinde, and E.E. Clothiaux, 2000: Cloud Droplet Size Distributions in Low-Level Stratiform Clouds. *Journal of the Atmospheric Sciences*, **57**, 295-311.

Nakajima, T., and M.D. King, 1990: Determination of the Optical Thickness and Effective Particle Radius of Clouds from Reflected Solar Radiation Measurements. Part I: Theory. *Journal of the Atmospheric Sciences*, **47**, 1878-1893.

Petty, G.W. *A First Course In Atmospheric Radiation, Second Edition.* Madison: Sundog Publishing, 2006.

Pilewskie, P. and S. Twomey, 1987: Cloud phase discrimination by reflectance measurements near 1.6 and 2.2 mm. *Journal of the Atmospheric Sciences*, **44**, 3419.

Platnick, S, M.D. King, S.A. Ackerman, W.P. Menzel, B.A. Baum, J.C. Riédi, and R.A. Frey, 2003: The MODIS Cloud Products: Algorithms and Examples from TERRA. *IEEE Transactions on Geoscience and Remote Sensing*, **41**, 459-473.

Ramsey, F. and Dan Schafer. *The Statistical Sleuth*. Duxbury Press, 2002.

Rogers, R.R. and M.K. Yau. *A Short Course in Cloud Physics, Third Edition.* Oxford: Butterworth Heinemann, 1989.

Schüller, L., J.L. Brenguier, and H. Pawlowska, 2003: Retrieval of microphysical, geometrical, and radiative properties of marine stratocumulus from remote sensing. *Journal of Geophysical Research*, **108**, doi:10.1029/2002JD002680, D002680.

Schüller, L., J.L. Brenguier, R. Bennartz, and J. Fischer, 2004: An Algorithm for the Retrieval of Droplet Number Concentration and Geometrical Thickness of Stratiform Marine Boundary Layer Clouds Applied to MODIS Radiometric Observations. *Journal of Applied Meteorology*, **44**, 28-44.

Segrin, M.S., J.A. Coakley Jr., and W.R. Tahnk, 2007: MODIS Observations of Ship Tracks in Summertime Stratus off the West Coast of the United States. *Journal of the Atmospheric Sciences*, **64**, 4330-4345.

Szczodrak, M., P.H. Austin, and P.B. Krummel, 2001: Variability of Optical Depth and Effective Radius in Marine Stratocumulus Clouds. *Journal of the Atmospheric Sciences*, **58**, 2912-2925.